FINAL REPORT

on

INVESTIGATION OF INSTABILITY, DYNAMIC FORCES, AND EFFECT OF DYNAMIC LOADING ON STRENGTH OF CAGES FOR THE BEARINGS IN THE HIGH PRESSURE OXYGEN TURBOPUMPS FOR THE SPACE SHUTTLE MAIN ENGINE
(Contract NAS8-36192, Task No. 117)

prepared for

NATIONAL AERONAUTICS AND SPACE
ADMINISTRATION
GEORGE C. MARSHALL SPACE FLIGHT CENTER
MARSHALL SPACE FLIGHT CENTER, AL

November 22, 1985

by

K. F. Dufrane, J. W. Kannel, T. L. Merriman,
and A. R. Rosenfield

BATTELLE
Columbus Division
505 King Avenue
Columbus, Ohio 43201

TABLE OF CONTENTS

TABLE OF CONTENTS (Continued)

LIST OF FIGURES

LIST OF TABLES

APPENDIX A

FINAL REPORT

on

INVESTIGATION OF INSTABILITY, DYNAMIC FORCES,
AND EFFECT OF DYNAMIC LOADING ON STRENGTH OF
CAGES FOR THE BEARINGS IN THE HIGH PRESSURE
OXYGEN TURBOPUMPS FOR THE SPACE SHUTTLE
MAIN ENGINE
(Contract NAS8-36192, Task No. 117)

prepared for

NATIONAL AERONAUTICS AND SPACE
ADMINISTRATION
George C. Marshall Space Flight Center
Marshall Space Flight Center, Al

November 22, 1985

INTRODUCTION

While the Space Shuttle main engine (SSME) has had demon-
strated success as a reusable power source, the bearings in the high
pressure oxygen turbopumps (HPOTP) continue to limit the service life
of the SSME to less than the desired goal of 27,000 seconds involving
55 starts between overhauls. Moves toward increasing the engine power
output have also placed increased demands on the HPOTP bearings and
have contributed to the life problem. In a continuing effort to assist
NASA in identifying means for extending bearing life, Battelle has
been conducting various related studies through a Task Order Agree-
ment. The current task was directed toward analyzing the instability
of the cage in the HPOTP bearings, frequencies and forces associated
with the instabilities, and the effect of cyclic forces on the strength
of the cage material.

Specific topics to be addressed in this task were:

- Ball/cage loadings as a function of radial load and misalignment
- Critical ball size variation to promote high ball-cage loads
- Critical friction conditions to promote cage instability
- Range of frequencies of cage motion during instabilities
- Ball/cage forces as a result of cage instabilities
- Effect of cyclic loading on cage strength
- Poisson's ratio for Armalon cage material
- Recommendations for improving SSME bearing performance

3

SUMMARY

Calculations were made of the magnitude of the ball/cage forces resulting from combined radial and axial loads. With an axial load of 4400 N (1000 lbs), the ball/cage pocket clearance is sufficient to accommodate the ball excursions produced by ball speed variation with radial loads to 3600 N (800 lbs). With loads beyond 3600 N (800 lbs), cyclic ball/cage forces are developed, the magnitude of which depend on the ball/race coefficient of friction. With a coefficient of friction of 0.2, the ball/cage forces are approximately 220 N (50 lbs). Although loads of this magnitude are well below an experimentally determined cage working strength of 1300 N (300 lbs), they may be sufficient to cause cage wear. On this basis, cage failures from overloading would appear to be the result of cage instabilities or excessive bearing overloads rather than from loads applied in normal operation.

Ball wear was found to be a minor factor in ball/cage loading. Wear on a single ball causes the applied loads to be carried by the surrounding unworn balls. The load on single ball decreases rapidly with wear; a radial wear of 0.025 mm (0.001 in.) is sufficient to remove all of its portion of the applied load. However, centrifugal loading continues to maintain a high contact pressure with the outer race, which is a likely significant factor in continuing the wear process for the unloaded ball. An oversized ball (presumably from wear of the other balls) carries a proportionally higher load. Resulting ball/cage forces are not excessive if the oversized ball remains within 6.3μm (250 μin.) of the complement. On a practical basis, a single oversized ball is not likely to exist for extended times because the higher loads and associated wear would be expected to reduce its size to that of the complement.

Analyses of cage stability have shown that the cage in general is only marginally stable, primarly because of the marginal ball/race lubrication conditions in comparison with conventionally lubricated bearings. The shear modulus and coefficient of friction at the ball/race

interface are both important factors in cage stability. Shear moduli
associated with PTFE films, or lower, result in stable cage operation.
As the shear moduli increases at the interface to that associated
with MoS_2 solid lubricants or steel-on-steel, the cage stability de-
creases. The impingement of liquid oxygen on the cage also influenced
stability. The constant force from the impingement in the direction
of rotation tended to promote stability. The frequency of cage oscil-
lations increase with increasing instability. Oscillating frequencies
to 33,000 Hz were predicted. Cage forces resulting from accelerations
associated with such high frequency oscillations were estimated to
exceed the cage compressive strength by a factor of two.

Experiments were performed to determine the effect of cyclic
loading on cage strength. A long-term working tensile load of approxi-
mately 1300 N (300 lbs) was found to be the likely maximum. Higher
loads, such as 1800 N (400 lbs), caused a decrease in cage tensile
strength after the 125,000-cycle testing period. Poisson's ratio
in compression was found to be highly dependent upon the direction
of the fiberglass plies. At room temperature the value was 0.15 with
the plies and 0.68 across the plies. At -196 C (-321 F), the value
with the plies was 0.20 (a bonding failure with the attached strain
gage prevented obtaining a reading across the plies).

CONCLUSIONS AND RECOMMENDATIONS

The results of the analyses conducted in this task have again demonstrated the critical need for improved lubrication in the HPOTP bearings. Lubricant films with low shear strength and low friction coefficients promote cage stability and decrease ball/cage forces during marginal operating conditions. Such lubrication also minimizes ball and race wear, which has been the principal longevity problem with these bearings. As the ball/race lubrication deteriorates, cage instability with high frequency oscillations and associated ball/cage loads occurs. A general performance deterioration follows with ball and race wear, compromised geometry, and increased likelihood of cage instability. Efforts to improve the long-term lubrication of the HPOTP bearings, such as with transfer films, are clearly warranted.

The analysis of the effect of combined bearing loads on ball/cage loads has identified a radial load of 3600 N (800 lbs) as the maximum for the current clearance of the balls and cage pockets. Elongating the cage pockets will help to reduce these loads if axial loads of greater than 3600 N (800 lbs) are to be encountered.

Liquid oxygen impinging on the cage in the direction of rotation was found to enhance cage stability. This suggests that further increases in the applied force in the cage rotating direction may be helpful for promoting stability. Because of the uncertainties in the knowledge of the fluid coupling forces and the ball/race traction conditions, such possible improvements will be best explored experimentally. However, the influence of the liquid oxygen impingement is secondary compared with the influence of the ball/race lubrication, and only corresponding second-order improvements are to be expected.

CAGE STABILITY ANALYSIS

Analyses Background

Ball-Race Interactions

External loading applied to an angular contact bearing develops forces at the ball-race interfaces. These forces, along with race geometry, speed, and centrifugal effects, produce the ball-race contact angles, ball-race contact pressures, lubricant film thickness (between balls and race), and to some extent, the spin and roll motions of the ball. The analysis of these ball-race interactions was the basis for the classical A. B. Jones' theory (1).

The Jones' approach involves first computing the spring rates for the ball-race contact regions. Next, values for the radial and axial deflections of the bearing are assumed. Using these assumed deflections in conjunction with the spring rates, radial and axial loads are computed and compared with the design bearing loads. The radial and axial deflections are adjusted (by a computer nesting procedure) to achieve the correct loads for static conditions. Centrifugal force effects are determined by adjusting the inner and outer race contact angles to achieve loading equilibrium.

Cage Dynamics

Under normal operation of most bearings, the cage can be considered to have six degrees of freedom. The motion of the cage is achieved as a result of the balls driving the cage or the cage driving the balls. The stability conditions of the cage are a result of the interactions during ball-cage impacts. As a result of these impacts, the kinetic energy of the cage is altered. For example, any slip of the ball on the race at impact will reduce the energy of the cage. Also, the friction coupling of the rolling ball to the cage during impact alters the cage energy. Under some conditions,

the energy of the cage will continue to increase until an instability occurs. Under other conditions, the energy of the cage is absorbed and the cage will be quite stable. The purpose of the BASDAP model is to sort out these stable or unstable conditions.

The BASDAP calculations are conducted in two steps:

Step 1:   The quasi-dynamic stresses of the type discussed under "Ball-Race Interactions of the Bearing" are computed.

Step 2.   The cage dynamic motions are computed using the ball-race forces and traction constants as inputs.

Cage stability can be accessed by analyzing plots of cage angle as a function of time. If the frequency of oscillation of the cage angle decreases with time, cage stability is implied. Conversely, if the frequency of oscillation increases, the cage is unstable.

New Cage Parameters Considered in This Task

Two new variables were considered in this task with regard to cage stability: the force on the cage from an impinging coolant flow of liquid oxygen and the influence of the ball-race friction coefficient. The friction conditions at the ball-cage and cage-race interfaces were considered only as parameters in a previous cage stability study (2).

Base Case with Updated Input Parameters

The computer analysis included several updated input parameters. Table 1 shows the current bearing data used in the analyses. Two points to notice are:

(1)   The new seals developed for the bearing are reported
      to be stiff enough to support some radial load. Accord-
      ingly, the radial load used in the analysis has been
      reduced to 1330N (300 lbs) (3).

(2)   The Armalon cage material properties, primarily the
      modulus, reflect new data from bearing materials stud-
      ies in May, 1985, (4), as well as Rocketdyne data.
      Traction data from the liquid nitrogen elastohydrody-
      namic film studies has also been added to the bearing
      analysis (5). Using these data, along with solid-film
      work that has been done at Battelle on another govern-
      ment project, engineering estimates have been made
      of the interface friction conditions. The accuracy
      of the cage stability predictions is directly dependent
      upon this limited knowledge of the interface friction
      conditions.

Figures 1 and 2 are plots of the bearing cage behavior using
the parameters in Table 1. Figure 3 indicates the coordinate system
used to define the cage location parameters for Figures 1 and 2.
Figure 3 shows that the angle β (beta) is the rotational angle of
the center of mass of the cage about the geometric center of the bear-
ing. The angle α (alpha) is the rotational angle of the cage about
its center of mass. $\dot{\alpha}$ (alphadot) and $\dot{\beta}$ (betadot) are the time deriva-
tives of alpha and beta, respectively. From examination of plots
of the above parameters the cage stability can be described as margi-
nal at best. Figure 1 indicates the cage motion does not dampen out
as it would in a very stable bearing. The predictions also show that
the oscillations do not build up into a complete instability, which
is somewhat encouraging. However, other combinations of operating
conditions and cage dimensions were identified in the March, 1984,
task which could drive the cage unstable (2).
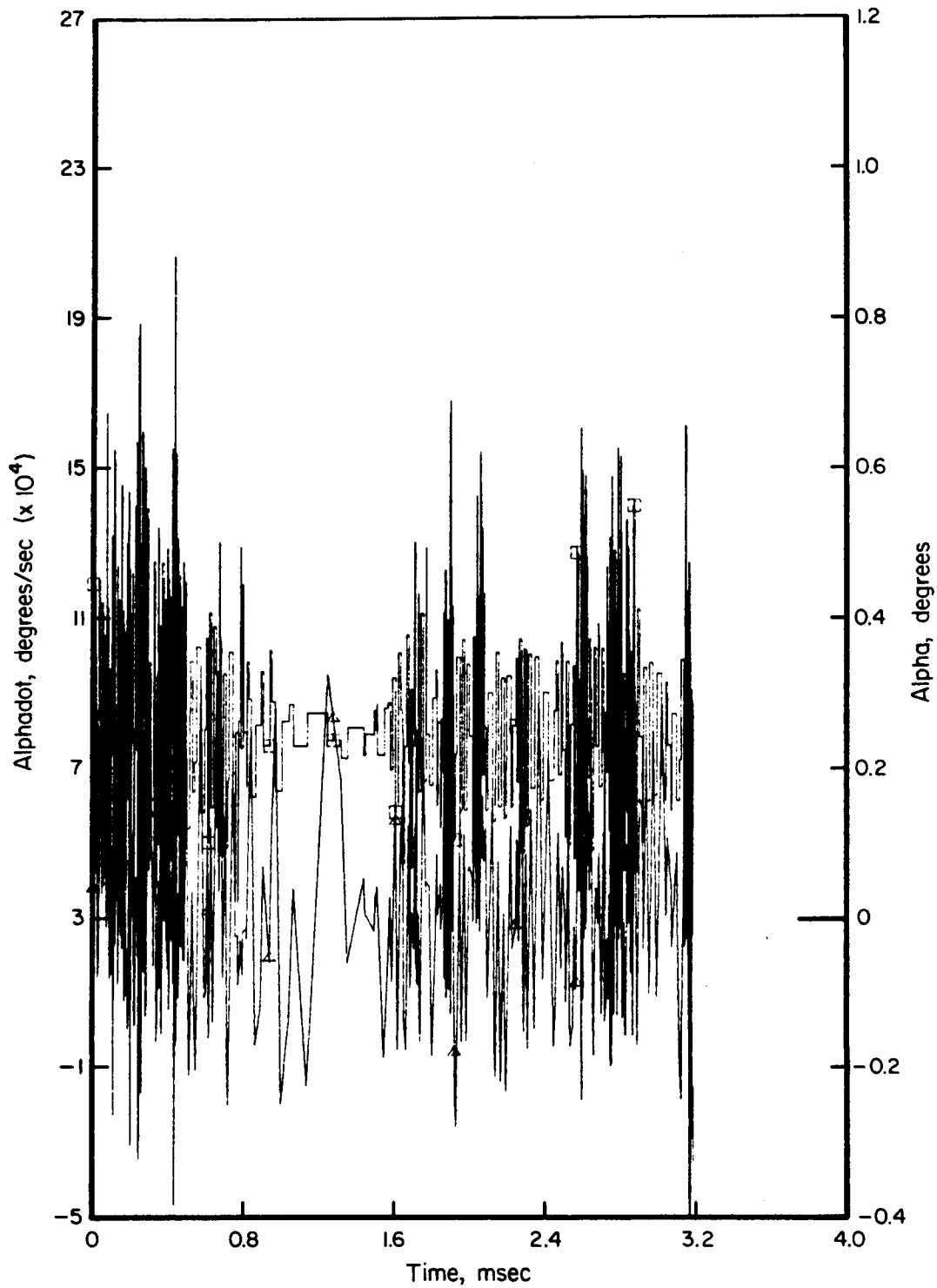
FIGURE 1. ALPHA (CAGE ROTATING ABOUT ITS CENTER OF MASS)
FOR NOMINAL OPERATING CONDITIONS

Axial Load   = 4448 N (1000 lb)
Cage-Race Friction   = 0.13
Cage-Race Radial Clearance   = 0.127mm (0.005 in.)
Speed   = 31,000 rpm
Radial Load   = 2669 (600 lb)
Ball-Cage Friction   = 0.30
Ball-Cage Radial Clearance   = 0.318mm (0.125 in.)
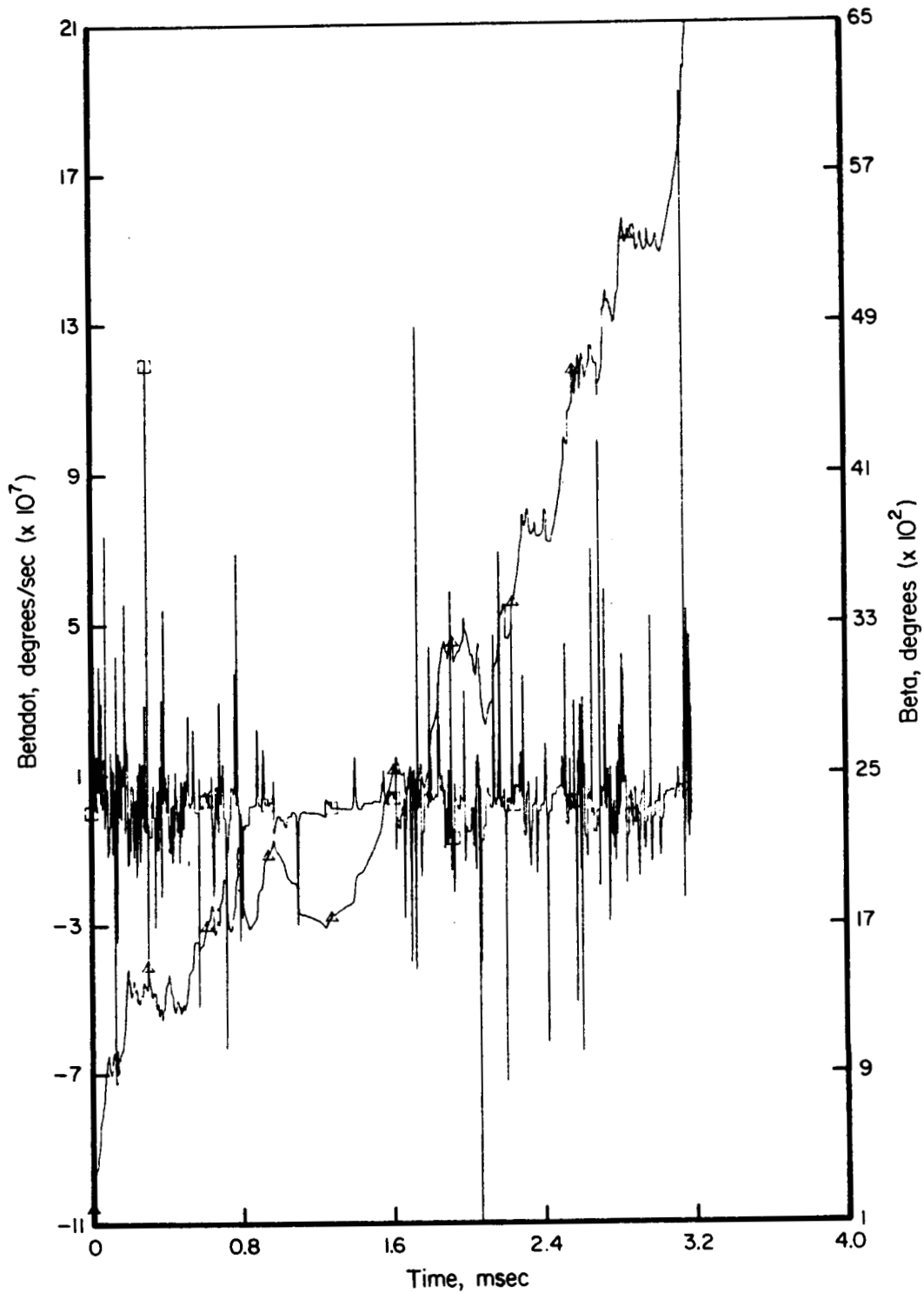
FIGURE 2. BETA (CAGE CENTER OF MASS ROTATING ABOUT THE BEARING
GEOMETRIC CENTER) FOR NOMINAL OPERATING CONDITIONS

Axial Load   = 4448 N (1000 lb)
Cage-Race Friction   = 0.13
Cage-Race Radial Clearance = 0.127 mm (0.005 in.)
Speed   = 31,000 rpm
Radial Load   = 2669 (600 lb)
Ball-Cage Friction   = 0.30
Ball-Cage Radial Clearance = 0.318 mm (0.125 in.)
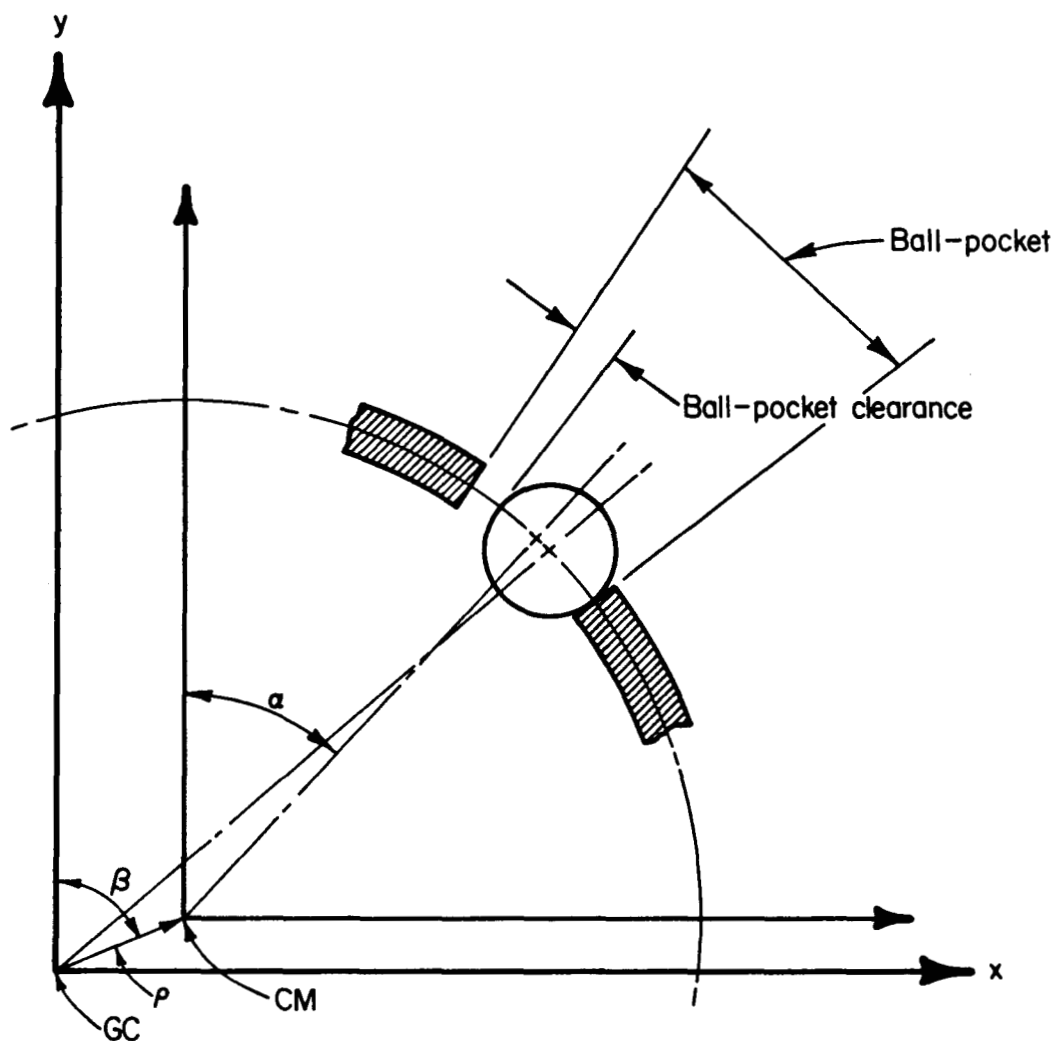
FIGURE 3. COORDINATE SYSTEM FOR CAGE-BALL LOCATIONS

GC   = Bearing Geometric Center
CM   = Cage Center of Mass
α (alpha) = Rotational Angle of Cage Around
              Cage Center of Mass
ρ (rho)   = Radial Displacement of Cage Center of
              Mass from Bearing Geometric Center
β (beta)   = Rotational Angle of Cage Center of
              Mass Around Bearing Geometric Center

TABLE 1.   NOMINAL BEARING PARAMETERS FOR NASA BEARING 007955,
HIGH PRESSURE OXYGEN TURBOPUMP, TURBINE END

Parameter	Units	Nominal Value
Number of balls	--	13
Ball radius	mm (inch)	6.35 (0.250)
Pitch radius	mm (inch)	40.51 (1.595)
Design contact angle	rad/degrees	0.36/20.5
Ball-cage radial clearance	mm (inch)	0.3175 (0.0125)
Cage-race radial clearance	mm (inch)	0.127 (0.005)
Outer race curvature	--	0.53
Inner race curvature	--	0.53
Axial load	N (lb)	4450 (1000)
Radial load	N (lb)	1330 (300)
Inner race speed	RPM	31000
Cage-race friction	--	0.13
Ball-cage friction	--	0.30
Ball-race friction	--	0.10
Base viscosity	cp	1
Viscosity under contact	cp	0.25×10^7
Pressure viscosity coefficient	1/Pascal (1/psi)	0.1×10^{-10} (0.1×10^{-6})
Operating temperature	C	-320
Lubricant specific gravity radial	--	1.14
Ball modulus	Pa (psi)	2.0×10^{11} (2.9×10^7)
Race modulus	Pa (psi)	2.0×10^{11} (2.9×10^7)
Cage compressive modulus	Pa (psi)	1.1×10^{10} (1.6×10^6)
Cage mass	gm (lb - sec^2/in.)	29.78 (1.73×10^{-4})

Effect of Liquid Oxygen Coolant Flow

The influence of the coolant flow of liquid oxygen on the bearing stability was considered by introducing a constant tangential force on the bearing cage into the computer model. The magnitude of the force expected as a result of a 2.11 kg/s (4.65 lb/sec) LOX flow was provided in literature from Rocketdyne and corresponds to a partial transfer of the fluid's momentum to the cage. Cases were run for coolant flows entering at rotational speeds both faster and slower than the cage speed. The results from plots such as Figures 1 and 2 are summarized below.

Tangential Force From LOX Coolant Flow	Cage Stability
N (lb)	
29 (6.6)	Stable
15 (3.3)	Marginally Stable
0 (0.0)	Marginally Stable
-15 (-3.3)	Stable
-29 (-6.6)	Marginally Stable

The following definitions were used to interpret the graphs:

- Completely unstable - high frequency oscillation,
- Marginally unstable - occasional oscillation build-up,
- Marginally stable - oscillations do not completely decay, but the cage does not go into high frequency oscillation,
- Stable - frequency and amplitude of oscillation decrease with time.

The LOX coolant jet shows a marked effect on stability. The force from this jet stabilized the cage motion when applied in the direction of bearing rotation. Applying the LOX jet force in a direction oppos-

ing the cage rotation caused a seemingly anomalous prediction by the BASDAP program. A small negative LOX jet force stabilized the cage motion, but a larger negative force produced marginally stable behavior. In view of these sensitivities, experimental verification may be warranted.

<div align="center">

The Effect of Ball-Race Traction and
Friction Coefficient on Cage Stability

</div>

Traction at the Ball-Race Interface of Liquid Lubricated Bearings

In cage-dynamics theories the balls are normally assumed to be in lubricated contact with the races. When the cage impacts the balls, the balls slip relative to the races. The reaction force developed by the balls is related to the slip rate imposed by the cage impact. The force is computed by a form of Newton's law of viscosity, or:

$$F_T = \int_A \mu \frac{\Delta v}{h} dA \tag{1}$$

where

A   is the contact area

μ is the viscosity of the lubricant

Δv is the slip velocity, and

h   is the thickness of the lubricant.

If h and Δv are assumed to be independent of A, equation (1) can be written:

$$F_T = C_{mu} \Delta v \tag{2}$$

$$C_{mu} = \int_A \frac{\mu}{h} dA \tag{3}$$

where C_{mu} is a constant related to lubricant and geometry.

Equation 2 is analogous to a dashpot equation in a spring-mass vibration problem. The larger the value of C_{mu} the less will be the energy absorption by the ball-race interface. In bearings where C_{mu} is very large, the cage motions tend to be unstable. In bearings where C_{mu} is small, the cage motions tend to be dampened by the ball slippage and the cage motions tend to be stable.

Equation 3 could be expressed in terms of a contact zone average viscosity (μ_{avg}) as:

$$C_{mu} = \frac{\pi ab}{h} \mu_{avg}, \tag{4}$$

where a and b are the dimensions of the ball/race contact region.

The average viscosity can be inferred from traction data for conditions similar to the conditions in a bearing. Combining Equations (2) and (4) results in:

$$\mu_{avg} = \frac{F_T}{\Delta v} \frac{h}{\pi ab}.$$

Extension to Solid Film Lubricated Bearings

If a rolling element bearing is unlubricated the film thickness term, h, tends to zero and C_{mu} becomes very large. For conditions involving thin or non-existent lubricant films, bearing life and the cage stability conditions become heavily dependent on solid surface layers on the balls and races. Three types of surface layers are:

- Oxide films,
- Pre-coated films such as sputtered MoS_2 layers,
- Transfer films from the bearing cage.

The extent of any of these three types of films existent in the bearing at any time is less well defined than in the case of films in a liquid lubricated bearing. Characterizing the traction-slip behavior of solid films is therefore more difficult than in the case of liquid films.

The traction in a solid film is related to the elastic tangential deflection of the interface between the ball and race (Figure 4). When the cage impacts a ball, the ball translational speed increases relative to the race. As a point on the surface of the race passes through contact, the surface is stretched as a result of the ball-race velocity differential. The extent of elastic deflection, ε, can be written:

$$\varepsilon = \frac{\Delta V}{V} x, \tag{6}$$

where

    ε is the surface deflection

  Δv is the differential velocity between ball and races

    v is the velocity of the race, and

    x is the distance from the inlet edge.

The local tractive force associated with ball-race slippage when a solid or liquid film is present can be written:

$$C \, \overline{F} = \overline{\varepsilon}, \tag{7}$$

where

    C is a matrix of influence coefficients

    $\overline{F}$ are point-tractions along the surface

    $\overline{\varepsilon}$ are the deformations given by Equation (6).
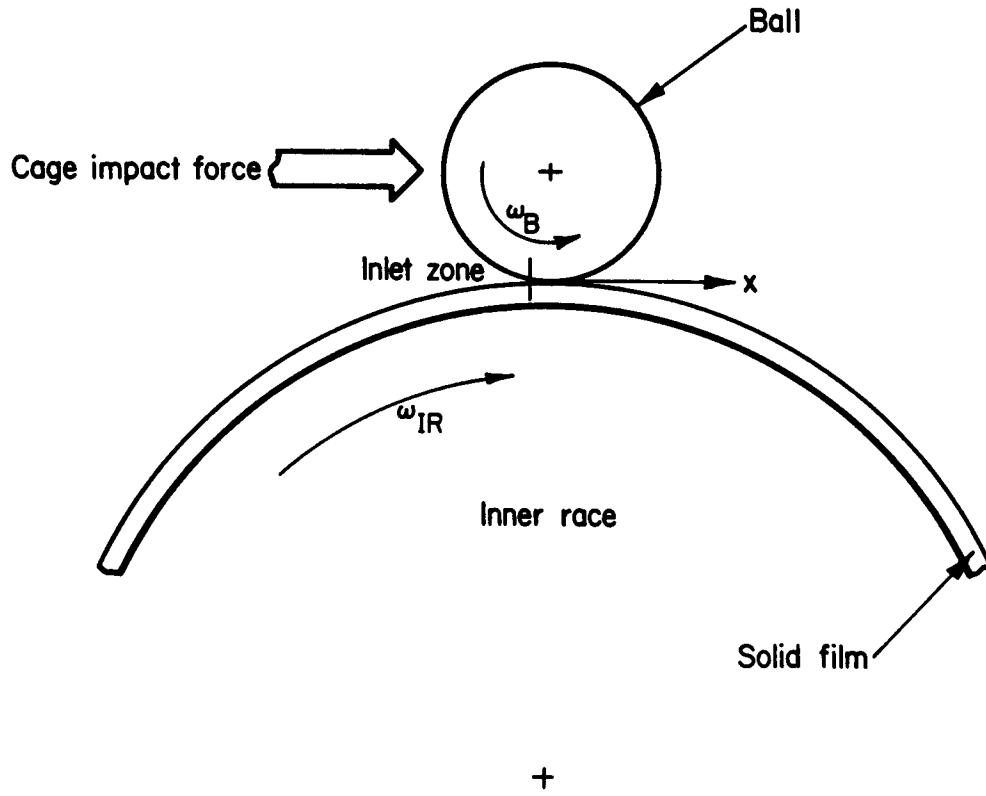
FIGURE 4.   NOMENCLATURE BALL RACE CONTACT

For the case of no surface films, the matrix coefficient can be written:

$$C_{ij} = - \frac{4(1-\nu^2)}{\pi E} \ln |r|, \qquad (8)$$

where

C_{ij} are the matrix coefficients

E is Young's modulus

ν is Poisson's ratio

r is the distance between the point traction load and the deformation.

Equation 7 is solved by dividing the interface into a discrete number of steps, such as 21, and writing 21 equations for point loads in terms of the known deformations. Equation 7 is solved for the point forces, which are the product of the point shear stresses times Δx. The one limitation applied to the computation is that:

$$\tau < fp, \qquad (9)$$

where

τ is shear stress

f is the friction coefficient

p is pressure.

When Equation 9 is violated the shear stress is given by:

$$\tau = fp. \qquad (10)$$

An equation similar to Equation 8 can be written for a solid film on the race surface (see Equation 5 of the paper in Appendix A).

Solid Film Traction in the HPOTP Bearing

A Battelle computer program ATCON (Analysis of Traction CONtact) has been used to evaluate the traction forces in the HPOTP bearing configuration. Typical contact conditions are:

$$p_0 = 1.92 \text{ GPa (279,000 psi)}$$
$$a = 1.46 \text{ mm (0.0576 in.)}$$
$$b = 0.25 \text{ mm (0.0099 in.)}$$

ATCON is based on line contact theory $(a \rightarrow \infty)$. The value of the relative radius R was adjusted to yield values of p_0 and b which were similar to those of the bearing. For the case of no solid film:

$$R = 7.62 \text{ mm (0.3 in.)}$$
$$p_0 = 1.9 \text{ GPa (277,000 psi)}$$
$$b = 0.254 \text{ mm (0.01 in.)}$$
$$\omega = 480 \text{ N/m (4,280 lb/in.)}.$$

Table 2 summarizes the stress conditions associated with soft surface films. The value of b was an input condition and was adjusted to yield approximately the same load for each condition.

Typical traction data are given in Figure 5 for the various solid film conditions and two levels of friction coefficient. The traction coefficient is the level of traction divided by the applied load. The most significant aspect of the curve is the slope near zero slip, since this reflects the traction resulting in small slip. At larger values of $\Delta v/v$ the traction coefficient approaches the coefficient of friction for pure sliding. In a bearing, only ball-to-ball radius variation would cause a slippage of the interfaces, or,

$$\Delta v/v = \Delta R/R,$$

TABLE 2. SUMMARY OF CONTACT PRESSURES ON SOLID FILMS

Load	γ	E_{film}	P_o	b
480 N/m	1	200 GPa	1.9 GPa	0.254 mm
481 N/m	0.01	2 GPa	1.69 GPa	0.305 mm
475 N/m	0.004	0.8 GPa	1.51 GPa	0.348 mm
471 N/m	0.002	0.4 GPa	1.35 GPa	0.394 mm
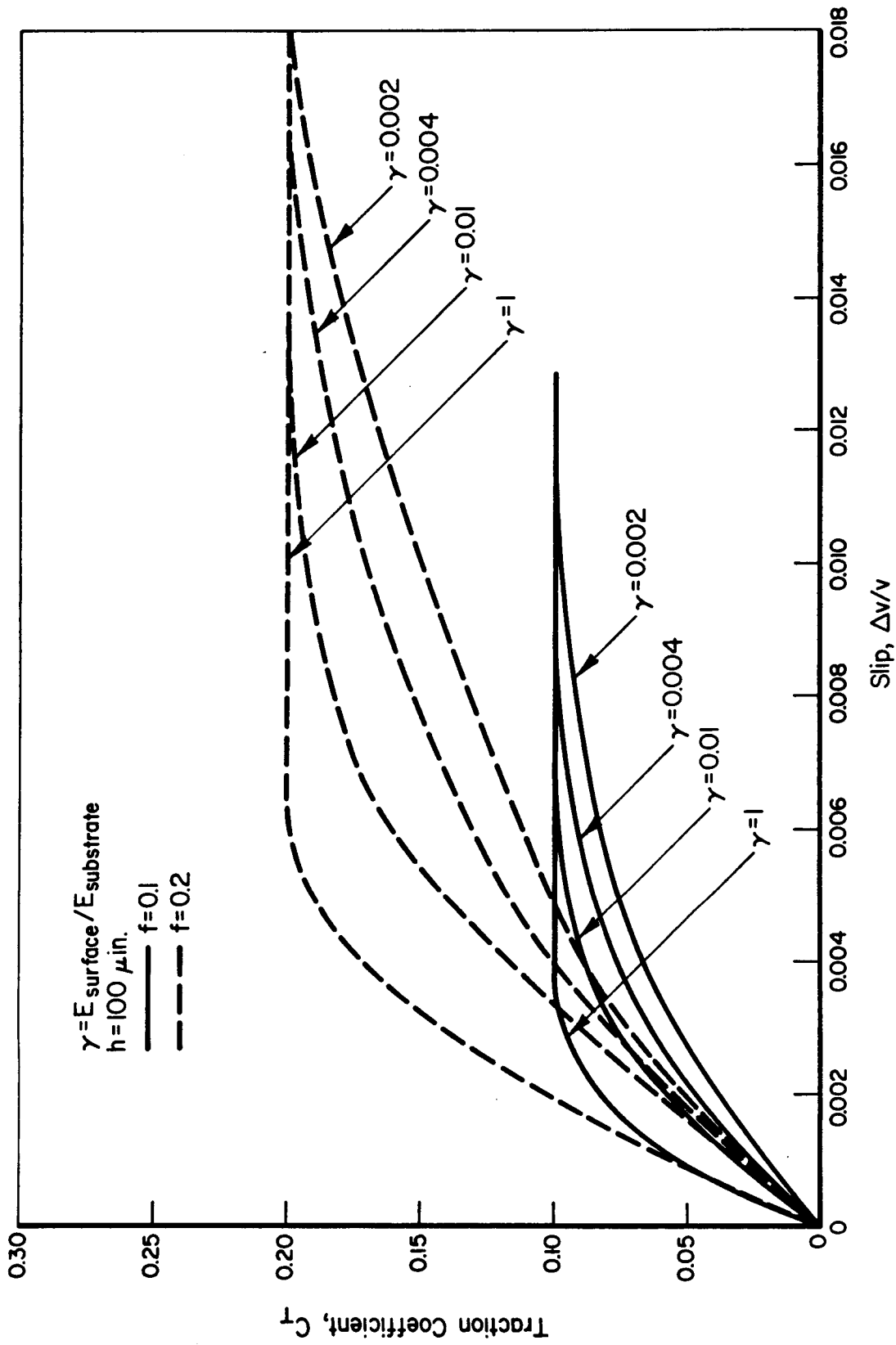
FIGURE 5. THEORETICAL TRACTION SLIP CURVES FOR VARIOUS COATINGS

TABLE 3. SUMMARY EFFECTIVE VISCOSITY COMPUTATIONS

Case	f	γ	$C_T(v/\Delta v)$	ave(Cp)	Simulation
1	0.1	1	51.	2.67×10^6	Steel-Steel
2		01	33.	1.73×10^6	MoS_2-Steel
3		004	26	1.36×10^6	---
4		002	19	1.0×10^6	PTFE-Steel
5	0.2	1	55.	2.88×10^6	Steel-Steel
6		01	34.	1.78×10^6	MoS_2-Steel
7		004	26.5	1.39×10^6	---
8		002	19.5	1.02×10^6	PTFE-Steel

where

R is the nominal ball radius of the group, and

ΔR is the variation in ball radius.

Based on the data of Figure 5 ball race, traction will be small provided $\Delta v/v > 0.0005$. Thus traction (and hence ball-cage forces) will be small provided the balls are matched within about 6.25μm (250μin.) on the diameter.

To use the data of Table 3 in bearing dynamics calculations it is helpful to use an effective viscosity parameter of the type given by Equation 5, based on the slope near zero slip. Equation 5 could be expressed:

$$\mu_{avg} = \frac{2p_o h}{3v} \left(\frac{C_T v}{\Delta v}\right) \qquad (11)$$

For a bearing the ball race velocity can be written:

$$v = \frac{1}{2} \frac{\omega_R}{R_p} \left[R_p^2 - (R_B \cos \beta)^2\right], \qquad (12)$$

where

ω_R is the angular velocity of the race

R_p is the pitch radius

R_B is the ball radius.

For the bearing of interest:

R_p = 40.5 mm (1.595 in.)

R_B = 6.35 mm (0.25 in.)

ω_R = 30,000 rpm (3,140 rad/sec)

$\beta \approx 15°$

p_o = 1.92 GPa (279,000 psi).

If it is assumed that h = 2.5μm (100μin.) Equation 11 appears as:

$$\mu_{avg} = 7.6 \times 10^{-3} \left(\frac{C_T v}{\Delta v}\right)\left(\frac{lb\text{-}sec}{in^2}\right) = 5.24 \times 10^4 \left(\frac{C_T v}{\Delta v}\right)(cp).$$

Despite the uncertainty of the contact zone phenomena, the variation in effective viscosities is not excessive. Since viscosity can range from 1 to 10^6 cp in the contact zone for liquid lubricants, a factor of 2 or 3 variation from one condition to another is not nearly as great as might be expected. The value of h used in the computations is unknown, but this parameter is arbitrary. In Equation 3 in the computation of C_{mu} the value of h is eliminated.

Cases 1 and 5 in Table 3 are for steel-versus-steel contacts. Cases 2 and 6 would be indicative of a soft film such as an MoS_2 coating. Cases 4 and 8 are an attempt to simulate a PTFE coating in the bearing.

Cage Stability Predictions with Inputs from the Solid Film Traction Analysis

The BASDAP computer program for prediction of cage stability was run with four of the effective viscosities presented in Table 3. Figures 6 through 9 are plots of the bearing cage behavior (alpha and alphadot as previously defined) for these effective viscosities. Table 4 summarizes the results. As lubricant conditions under the ball degrades (higher effective viscosities), it becomes more difficult for the ball to slip on the race. During ball-cage impacts under their conditions, energy of the cage is not absorbed at this interface through the lubricant shear mechanism. The result is that the cage stability degrades in parallel with a degraded lubricant condition at the ball-race interface.

FIGURE 6.   ALPHA (CAGE ROTATING ABOUT ITS CENTER OF MASS)
FOR SIMULATION OF PTFE-STEEL FILM AND BALL-RACE
FRICTION = 0.1

Axial Load   = 4448 N (1000 lb)
Cage-Race Friction   = 0.13
Cage-Race Radial Clearance   = 0.127mm (0.005 in.)
Speed   = 31,000 rpm
Radial Load   = 1330 N (300 lb)
Ball-Cage Friction   = 0.30
Ball-Cage Radial Clearance   = 0.318mm (0.125 in.)
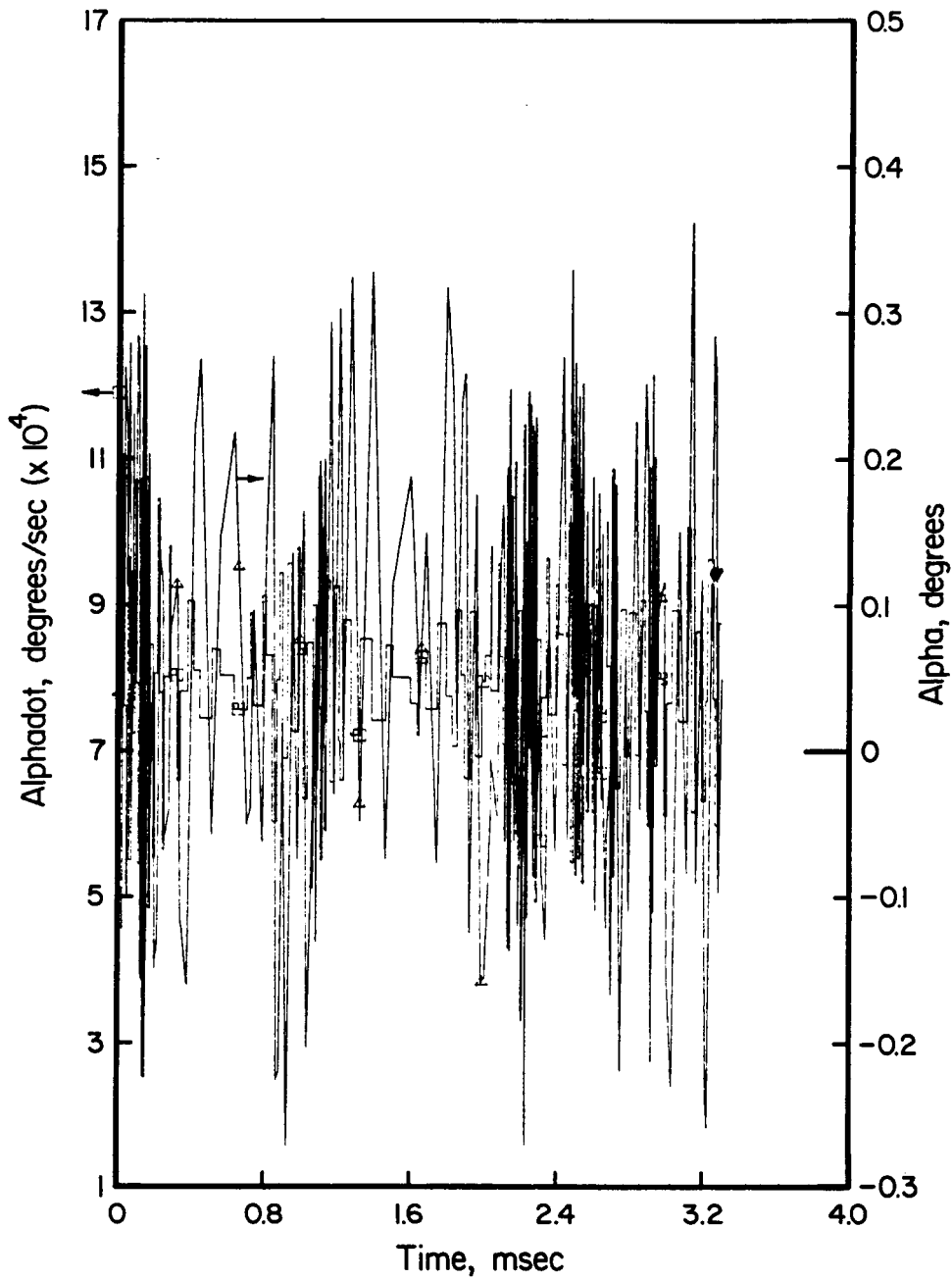
FIGURE 7. ALPHA (CAGE ROTATING ABOUT ITS CENTER OF MASS) FOR SIMULATION OF MoS_2-STEEL FILM AND BALL-RACE FRICTION = 0.1

Axial Load   = 4448 N (1000 lb)
Cage-Race Friction   = 0.13
Cage-Race Radial Clearance   = 0.127mm (0.005 in.)
Speed   = 31,000 rpm
Radial Load   = 1330 N (300 lb)
Ball-Cage Friction   = 0.30
Ball-Cage Radial Clearance   = 0.318mm (0.125 in.)
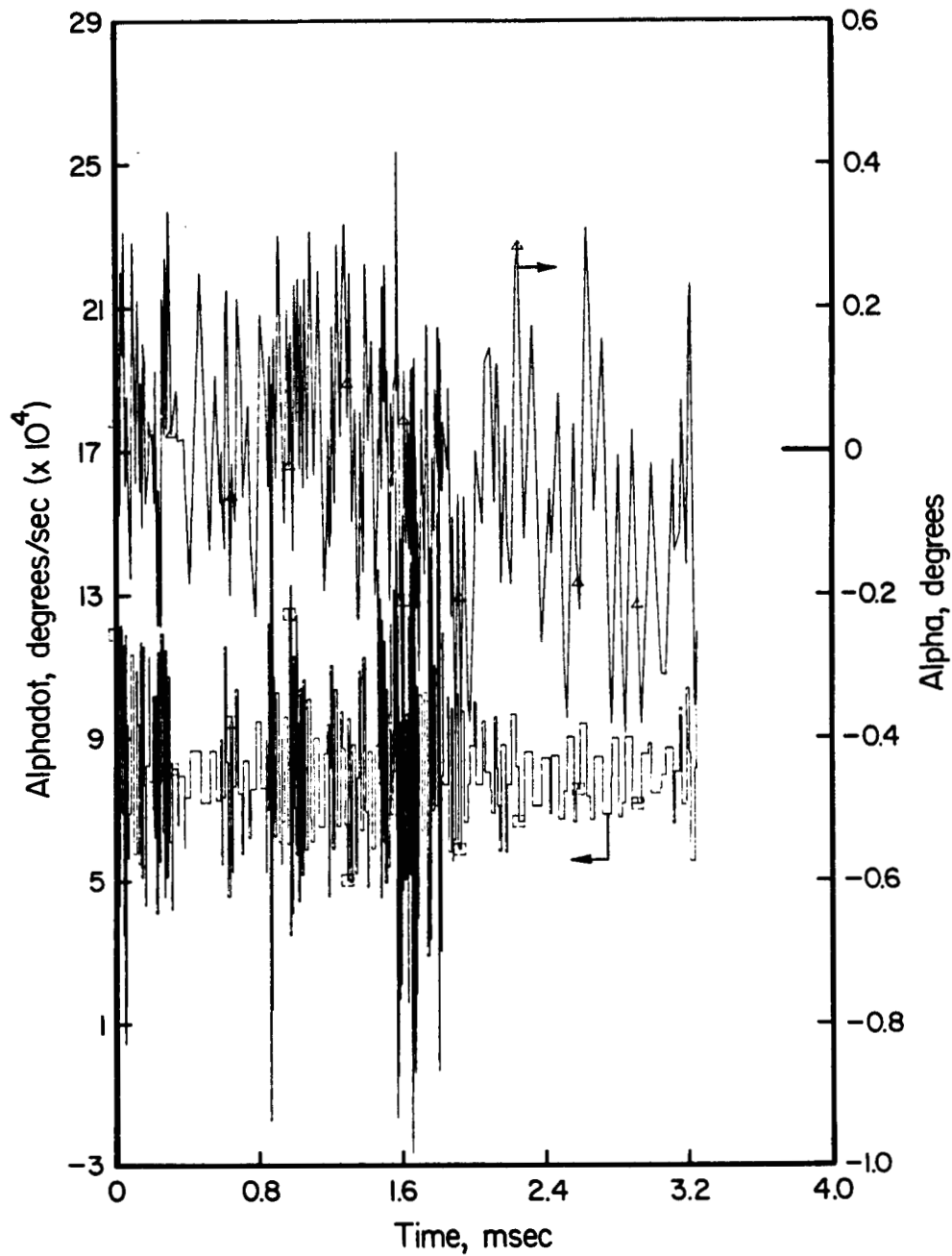
FIGURE 8.   ALPHA (CAGE ROTATING ABOUT ITS CENTER OF MASS)
FOR SIMULATION OF STEEL-STEEL INTERFACE AND
BALL-RACE FRICTION = 0.1

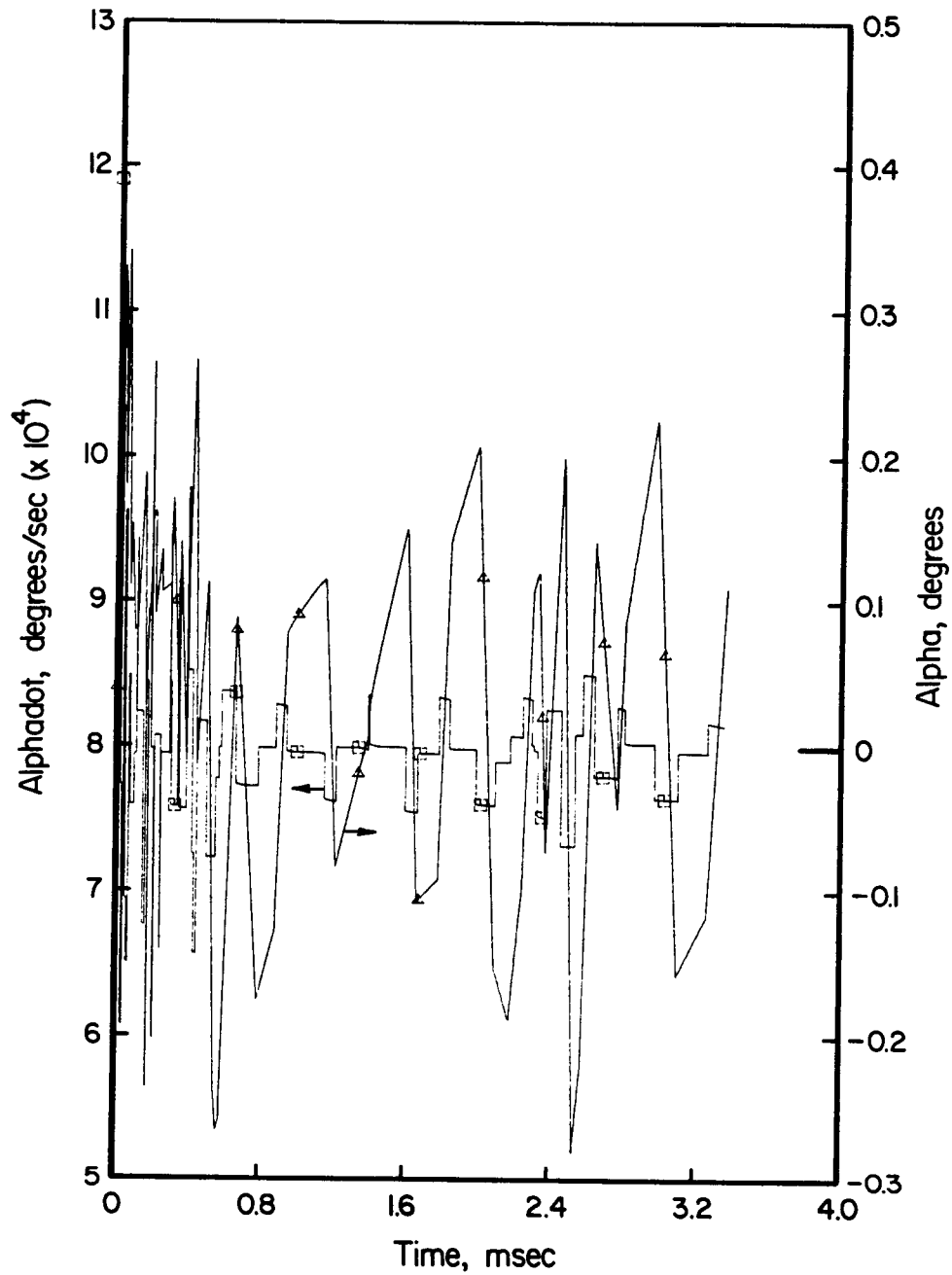|	
Axial Load	= 4448 N (1000 lb)
Cage-Race Friction	= 0.13
Cage-Race Radial Clearance	= 0.127mm (0.005 in.)
Speed	= 31,000 rpm
Radial Load	= 1330 N (300 lb)
Ball-Cage Friction	= 0.30
Ball-Cage Radial Clearance	= 0.318mm (0.125 in.)

FIGURE 9. ALPHA (CAGE ROTATING ABOUT ITS CENTER OF MASS)
FOR SIMULATION OF STEEL-STEEL INTERFACE AND
BALL-RACE FRICTION = 0.2

```
Axial Load                 = 4448 N (1000 lb)
Cage-Race Friction         = 0.13
Cage-Race Radial Clearance = 0.127mm (0.005 in.)
Speed                      = 31,000 rpm
Radial Load                = 1330 N (300 lb)
Ball-Cage Friction         = 0.30
Ball-Cage Radial Clearance = 0.318mm (0.125 in.)
```
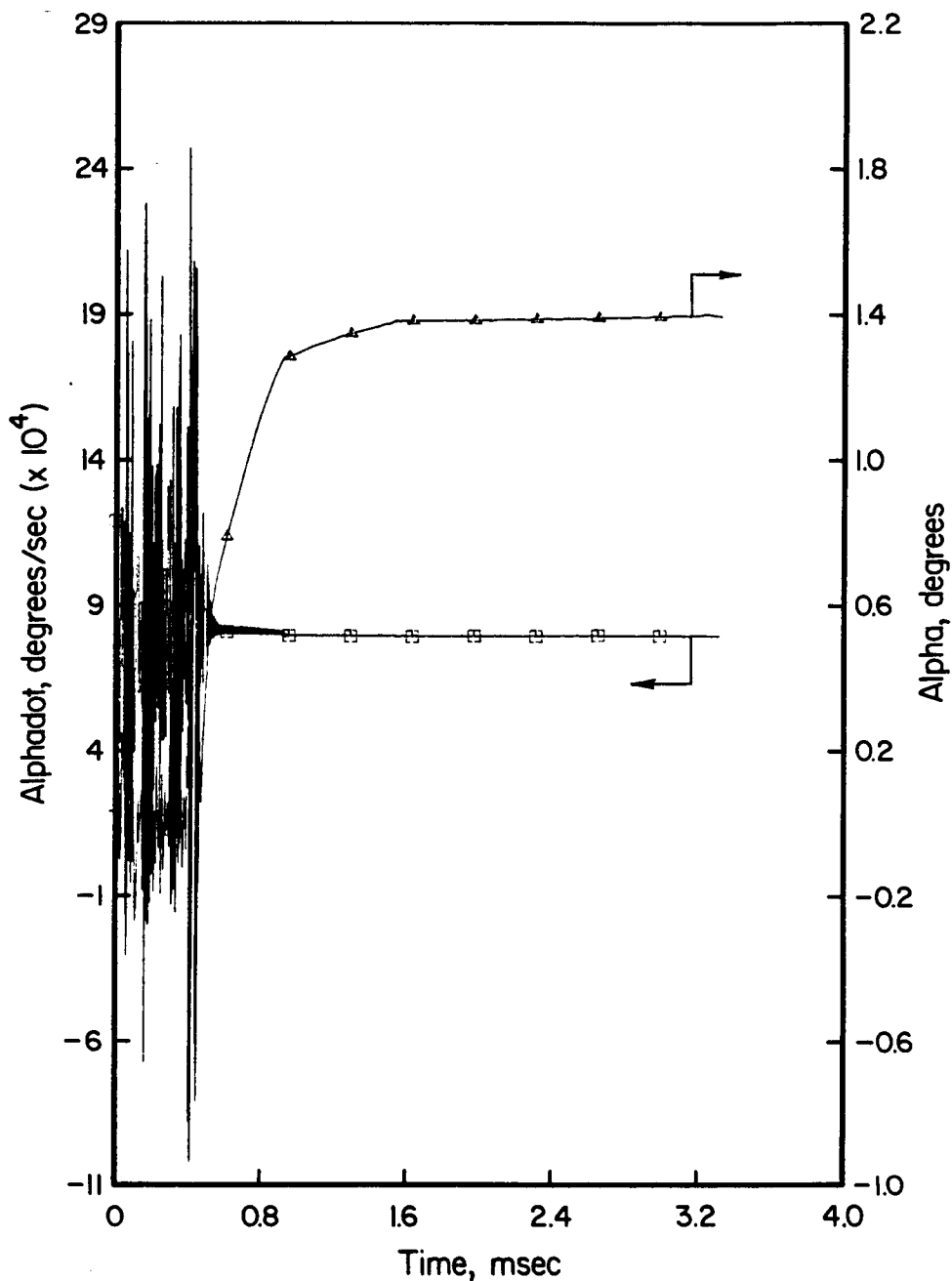
TABLE 4. BASDAP CAGE STABILITY PREDICTIONS FOR VARIOUS
VISCOSITIES AT THE BALL-RACE INTERFACE

Ball-Race Friction Coefficient	Simulation	μ_{avg}	Cage Stability
0.1	PTFE-Steel	1.00e+6	Stable
0.1	MoS_2-Steel	1.73e+6	Marginally Stable
0.1	Steel-Steel	2.67e+6	Marginally Stable
0.2	Steel-Steel	2.88e+6	Completely Unstable

The Effect of Shaft Speed on Cage Stability

The effect on cage stability of varying the shaft speed
was studied at 27,000 to 33,000 rpm. The nominal case around which
the speed parameter was varied was the base case of Table 1 with the
apparent viscosity from Table 3, which gave the most stable plot (appar-
ent viscosity = 1.0×10^6cp). The results showed no quantitative
jumps in stability. The plots of cage motion were slightly more sta-
ble at the lowest speed.

Ball-Cage Forces During Instability

The ball-cage forces which arise as a result of cage insta-
bilities were considered in the March, 1984 report on pages 26 and
27 (2). The analyses given there also apply to the cases given in
the current task. The instantaneous accelerations that occur when
the cage is oscillating in an unstable mode result in cage forces
estimated to be about twice the 5900 N (1300 lb) compressive strength
of the cage.

Frequencies of Cage Motion

The frequencies of cage motion predicted using the compter models are given in Table 5.

TABLE 5.   RANGE OF FREQUENCIES* OF CAGE MOTION DURING INSTABILITIES

Shaft Speed of Bearing	520 Hz
Nominal Ball-Group Speed**	220 Hz
BASDAP Predictions for whirl:	
Stable Bearing	650 Hz
Marginally Stable	2000-6100 Hz
Marginally Unstable	33300 Hz
Kingsbury Cage Whirl Mode Estimate***	27300 Hz

*The frequencies listed here are not the mechanical resonances of the cage, rather they reflect the response of the ball-cage-race system. For a complete discussion of cage instability see references 6 and 7.

**Under conditions given in Table 1, as predicted from A. B. Jones (1) equation using ball spin calculated by BASDAP computer program

***Limit estimate (after Kingsbury, reference 8).

The frequencies of cage motion are well above the frequency of the nominal ball group speed. As the cage stability drops to marginal there is an order of magnitude increase in frequency (6100 Hz). If the cage degrades one step farther to marginally unstable, the frequency of motion rises to 33,300 Hz. This frequency is the same order of magnitude as the upper limit of the cage whirl mode predicted from the ball spins and ball pocket clearance (Kingsbury).

Ball-Cage Interactions During Stable Operation

Another major area considered under this task was the ball-cage loading both under stable conditions and with ball size variations. Figure 10 shows the nomenclature used to describe the bearing for this discussion. Thirteen representative locations around the bearing were used, referred to by ball number. Figure 10 also shows the relationship of the externally applied loads to the ball locations. At position No. 1 the ball is under maximum combined load.

Effect of Radial Load

Table 6b gives the contact pressures and contact angles calculated by BASDAP for the nominal bearing parameters of Table 1. An average normal force at the ball-race interface can be calculated from the ball contact pressures. This force in conjunction with the ball-race friction coefficient determines the maximum value of ball-cage force under stable operating conditions. Figure 11 shows the maximum value of ball-cage force plotted for several radial loads. A similar plot was prepared for several axial loads in reference 1, page 25.

There are several possibilities for estimating the ball-race friction coefficient. Traction studies performed at Battelle using liquid nitrogen as the lubricant indicated traction coefficients of 0.02 to 0.06. These measurements did not include the effect of transfer films. Solid film transfer studies at Battelle at room temperature have indicated a ball-race friction coefficient of 0.15, but did not include hydrodynamic film effects. Palmgren (9) indicated a friction coefficient of 0.10 for a ball with combined rolling and sliding between two flat plates for dry contact. He reported a friction coefficient of 0.08 for a lubricated contact. The ball-race friction coefficient for the HPOTP bearing at cryogenic temperature might be estimated from the above data at 0.1. In any case, the ball-cage force that arises from a single ball pushing or lagging under

Top dead
center

27.7°   332.3°

55.4°   304.6°

53.1°   276.9°

110.8°   249.2

138.5°   221.5°

166.2°   193.8°
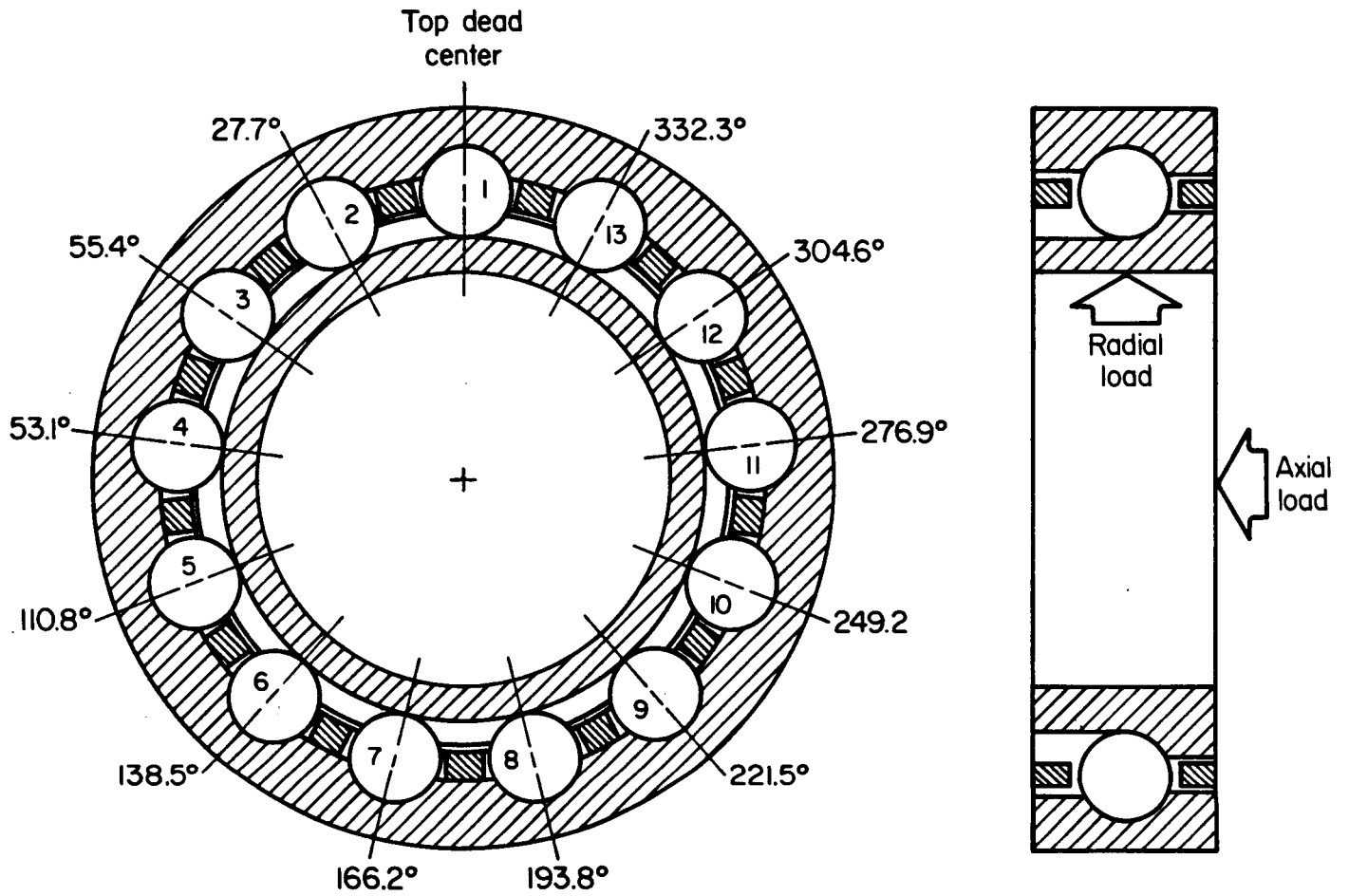
Radial
load

Axial
load

FIGURE 10. BEARING NOMENCLATURE

TABLE 6. BEARING PARAMETERS CALCULATED BY BASDAP SHOWING EFFECT OF RADIAL LOAD
AXIAL LOAD = 4450N (1000 lb), SHAFT SPEED = 31000 rpm

a. radial load = 0N (0 lb)

Contact Angle		Contact Pressure (psi)	
Inner (Deg)	Outer (Deg)	Inner	Outer
31.922	16.058	0.2441E + 06	0.2635E + 06
31.922	16.058	0.2441E + 06	0.2635E + 06
31.922	16.058	0.2441E + 06	0.2635E + 06
31.922	16.058	0.2441E + 06	0.2635E + 06
31.922	16.058	0.2441E + 06	0.2635E + 06
31.922	16.058	0.2441E + 06	0.2635E + 06
31.922	16.058	0.2441E + 06	0.2635E + 06
31.922	16.058	0.2441E + 06	0.2635E + 06
31.922	16.058	0.2441E + 06	0.2635E + 06
31.922	16.058	0.2441E + 06	0.2635E + 06
31.922	16.058	0.2441E + 06	0.2635E + 06
31.922	16.058	0.2441E + 06	0.2635E + 06
31.922	16.058	0.2441E + 06	0.2635E + 06

b. radial load = 1330N (300 lb)

| Contact Angle		Contact Pressure (psi)	
Inner (Deg)	Outer (Deg)	Inner	Outer
30.205	17.565	0.2707E + 06	0.2791E + 06
30.378	17.417	0.2677E + 06	0.2773E + 06
30.888	16.974	0.2594E + 06	0.2723E + 06
31.692	16.258	0.2473E + 06	0.2653E + 06
32.669	15.363	0.2339E + 06	0.2580E + 06
33.585	14.498	0.2224E + 06	0.2520E + 06
34.148	13.956	0.2157E + 06	0.2488E + 06
34.148	13.956	0.2157E + 06	0.2488E + 06
33.585	14.498	0.2224E + 06	0.2520E + 06
32.669	15.363	0.2339E + 06	0.2580E + 06
31.692	16.258	0.2473E + 06	0.2653E + 06
30.888	16.974	0.2594E + 06	0.2723E + 06
30.378	17.417	0.2677E + 06	0.2773E + 06
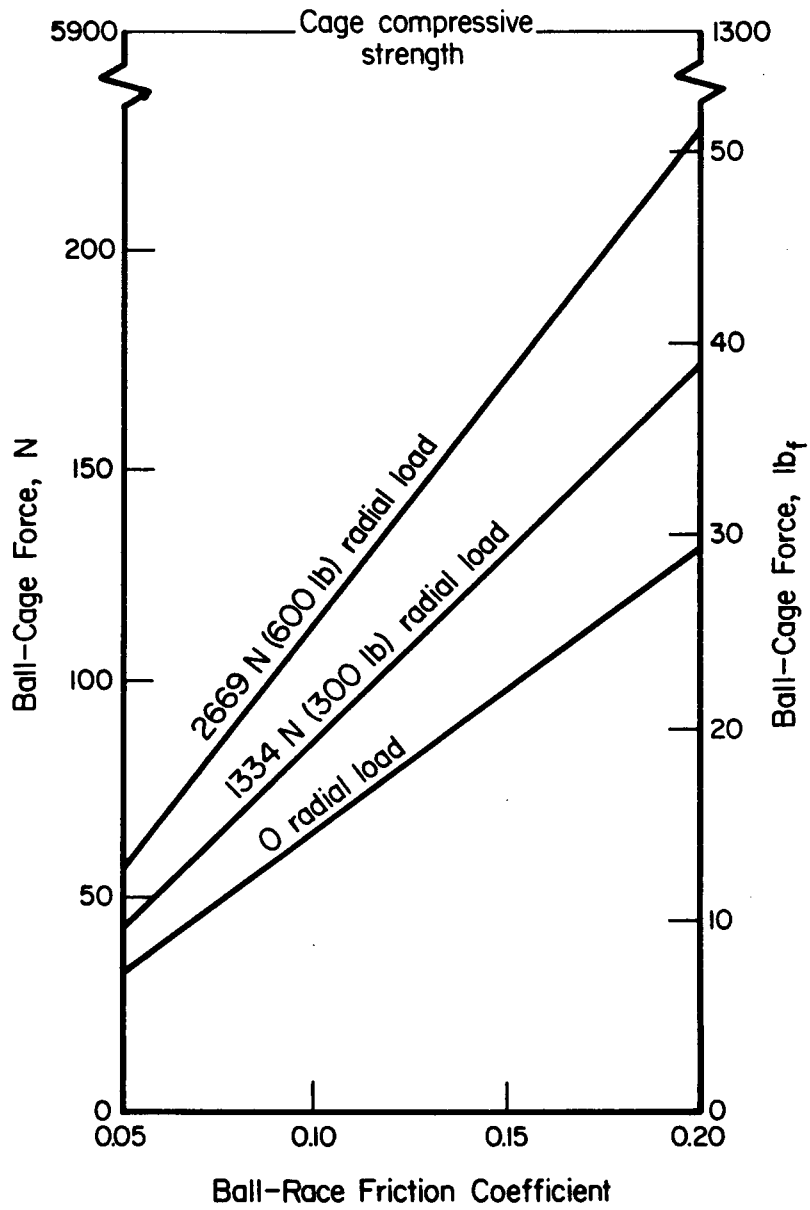
FIGURE 11. MAXIMUM BALL-CAGE FORCES, PREDICTED BY BASDAP,
            UNDER STABLE OPERATING CONDITIONS, FOR VARIOUS
            RADIAL LOADS.

            Axial Load - 4450 N (1000 lb)
            Shaft Speed = 3100 rpm

stable operating conditions is well below the ultimate strength of
the cage in either tension, 6900 N (1600 lb), or compression, 5900 N
(1300 lb).

The ball-cage impact will occur only under the condition
when a ball excursion about the average ball group speed is sufficient
to exceed ball-pocket clearance. Figure 12 shows the ball excursions
under stable operating conditions as calculated by BASDAP for the
most current data given in Table 1. Figure 12 shows that the excur-
sions due to the contact angle variation will exceed the diametral
ball-cage clearance, 0.635 mm (0.025 in.), for radial loads greater
than 3560 N (800 lb).

Effect of Worn Balls

The effects of ball size variation on ball excursions and
ball-cage loads were also examined in this task. As a ball becomes
increasingly undersized through wear, it will continue to carry load
up to some limiting point depending on the extent of ball-race deflec-
tion. With radial wear of 0.0025 mm (0.0001 in.) a single undersized
ball will carry 82 percent of its normal load. At 0.013 mm (0.0005 in.)
radial wear the ball carries only 5 percent of its normal load and
moves to lower contact angles on the outer race. At 0.025 mm (0.001 in.)
radial wear the worn ball carries none of the load. Table 7 shows
the contact angles and contact pressures assuming one worn ball at
position No. 1, with a radial wear of 0.025 mm (0.001 in.). The worn
ball drops to a zero contact angle on the outer race. The contact
pressure on the outer race is strictly from centrifugal force. The
centrifugal force at 31,000 rpm is significant, however, and the con-
tact pressure at the outer race drops only 15 to 20 percent from its
loaded contact pressure. Ball-cage forces continue to occur as a
reaction of LOX drag on the ball, Figure 13. Ball wear can thus
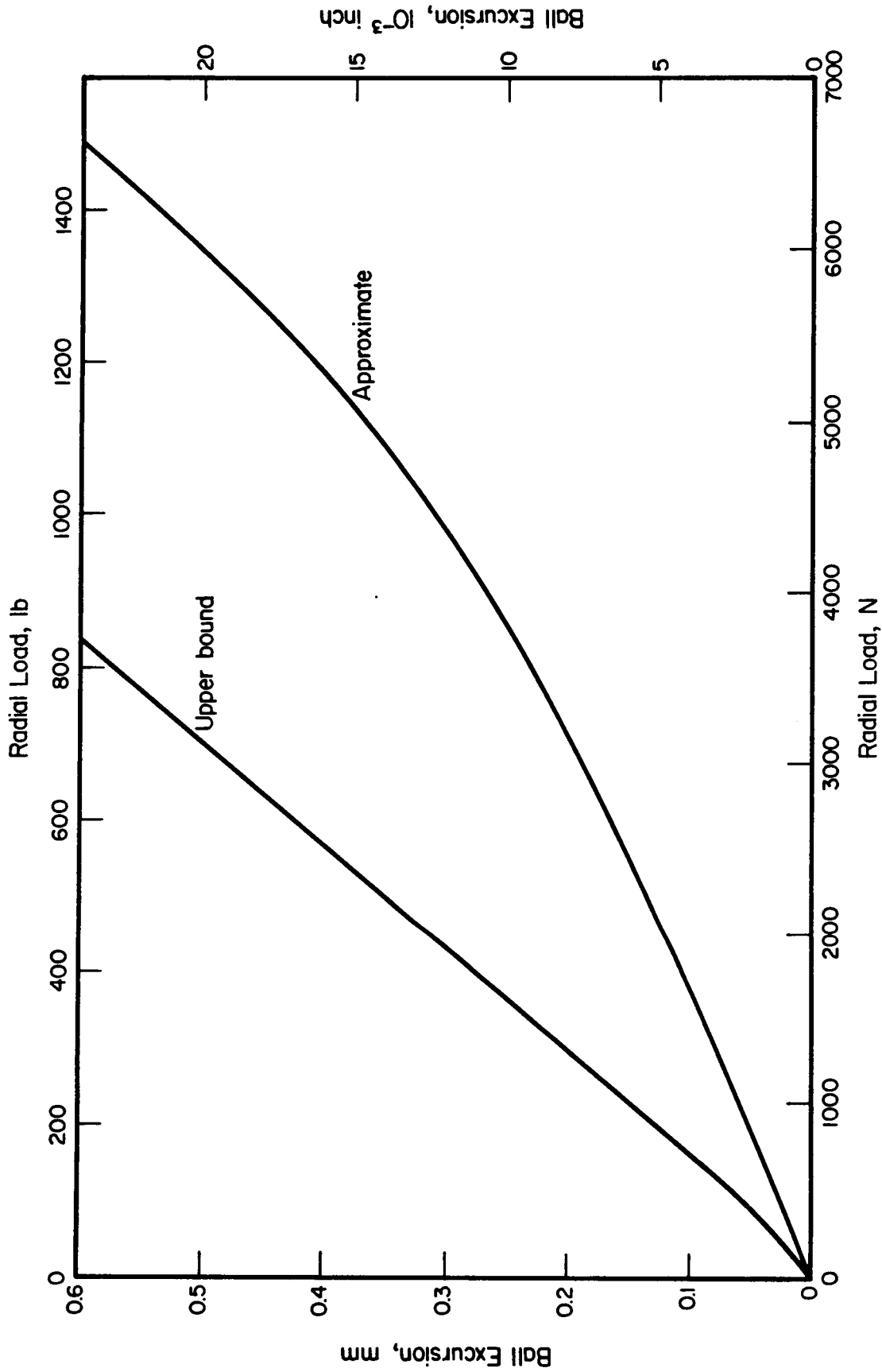occur even after the ball is no longer contacting the inner race.

FIGURE 12. BALL EXCURSIONS AS PREDICTED BY BASDAP FOR NOMINAL OPERATING CONDITIONS

TABLE 7. BEARING PARAMETERS CALCULATED BY BASDAP SHOWING EFFECT
OF ONE 12.4 mm (0.488 in.) DIAMETER BALL AT POSITION ONE.
AXIAL LOAD = 4450 N (1000 lb), SHAFT SPEED = 31000 rpm,
RADIAL LOAD = 1330 N (300 lb).

Contact Angle		Contact Pressure (psi)	
Inner (Deg)	Outer (Deg)	Inner	Outer
0.000	0.000	0.4715E + 01	0.2122E + 06
29.333	18.765	0.2933E + 06	0.2934E + 06
30.031	18.196	0.2798E + 06	0.2847E + 06
31.217	17.181	0.2597E + 06	0.2724E + 06
32.807	15.746	0.2369E + 06	0.2595E + 06
34.443	14.195	0.2167E + 06	0.2492E + 06
35.507	13.148	0.2048E + 06	0.2436E + 06
35.507	13.148	0.2048E + 06	0.2436E + 06
34.443	14.195	0.2167E + 06	0.2492E + 06
32.807	15.746	0.2369E + 06	0.2595E + 06
31.217	17.181	0.2597E + 06	0.2724E + 06
30.031	18.196	0.2798E + 06	0.2847E + 06
29.333	18.765	0.2933E + 06	0.2934E + 06

f ≤ 53 N (12 lb)

Fluid drag, ≥ 53 N (12 lb)

ω_{ball}

Ball-cage force, 53N (12 lb)
(estimated from horsepower
requirement for churning and
fluid drag)

18 N (4 lb) (calculated with
friction coefficient=0.3)

819 N (184 lb) (calculated
from contact pressure)
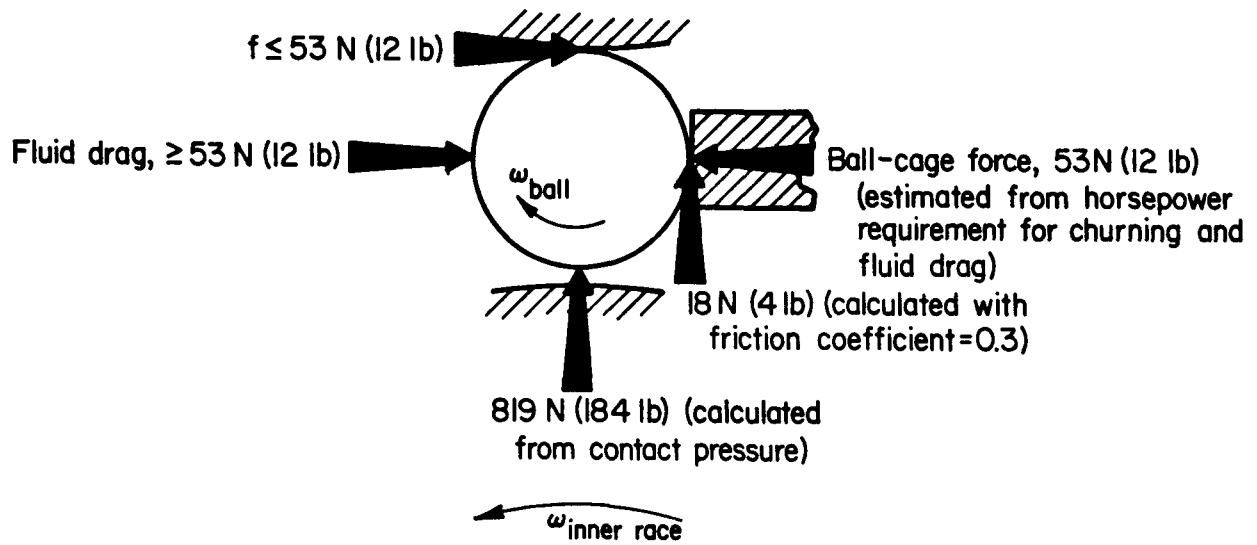
$\omega_{inner\ race}$

FIGURE 13.   SCENARIO OF FORCES ON A BALL THAT HAS
DROPPED OUT OF CONTACT DUE TO WEAR

EFFECT OF CYCLIC LOADING ON CAGE STRENGTH

Dynamic cage forces during instability and excessive ball speed variation apply cyclic forces to the cage. Measurements were needed of the effect of cyclic loads on cage strength to assess the potential deterioration of the cage from such cyclic loads. Sections of actual unused cages were subjected to cyclic tensile forces and then pulled to tensile failure. A comparison was made with the results of tensile tests on identical cage sections not subjected to cyclic forces.

Cage Loading Procedure

Four unused cages removed from new bearings that were rejected because of corrosion damage to the races during storage were used for the study. The cages were sectioned by cutting every fourth ball pocket to produce three specimens with two ball pockets intact and a fourth specimen with three ball pockets. The specimens were mounted as shown schematically in Figure 14. The radius of the support base matched that of the inner radius of the cage to avoid bending. The anchor pin was positioned so that the movable pin was pivoted at the position of the cage center so that the forces applied to the cage would directly simulate those applied in tension by the balls. The diameter of both the anchor pin and the movable pin was 12.7 mm (0.500 in.) to match that of the balls.

The specimen support fixture shown in Figure 13 was assembled for direct mounting in a conventional 44,000 N (10 KIP) fatigue testing machine. The specimen fixture was designed so that it could be submerged into a dewar flask of liquid nitrogen. The nitrogen level was detected and controlled by thermocouples placed to maintain a minimum depth of 127 mm (5 in.) above the cage specimen. The specimen support base was connected to the hydraulic actuator of the fatigue machine. The movable pin was connected to the load cell of the fatigue machine to apply and detect the opposing force on the cage.

Cyclic
load

To
load
cell

Slot for
movable
pin

Movable
pin

Pivot at cage
center

Anchor
pin

Cage section with
two ball pockets

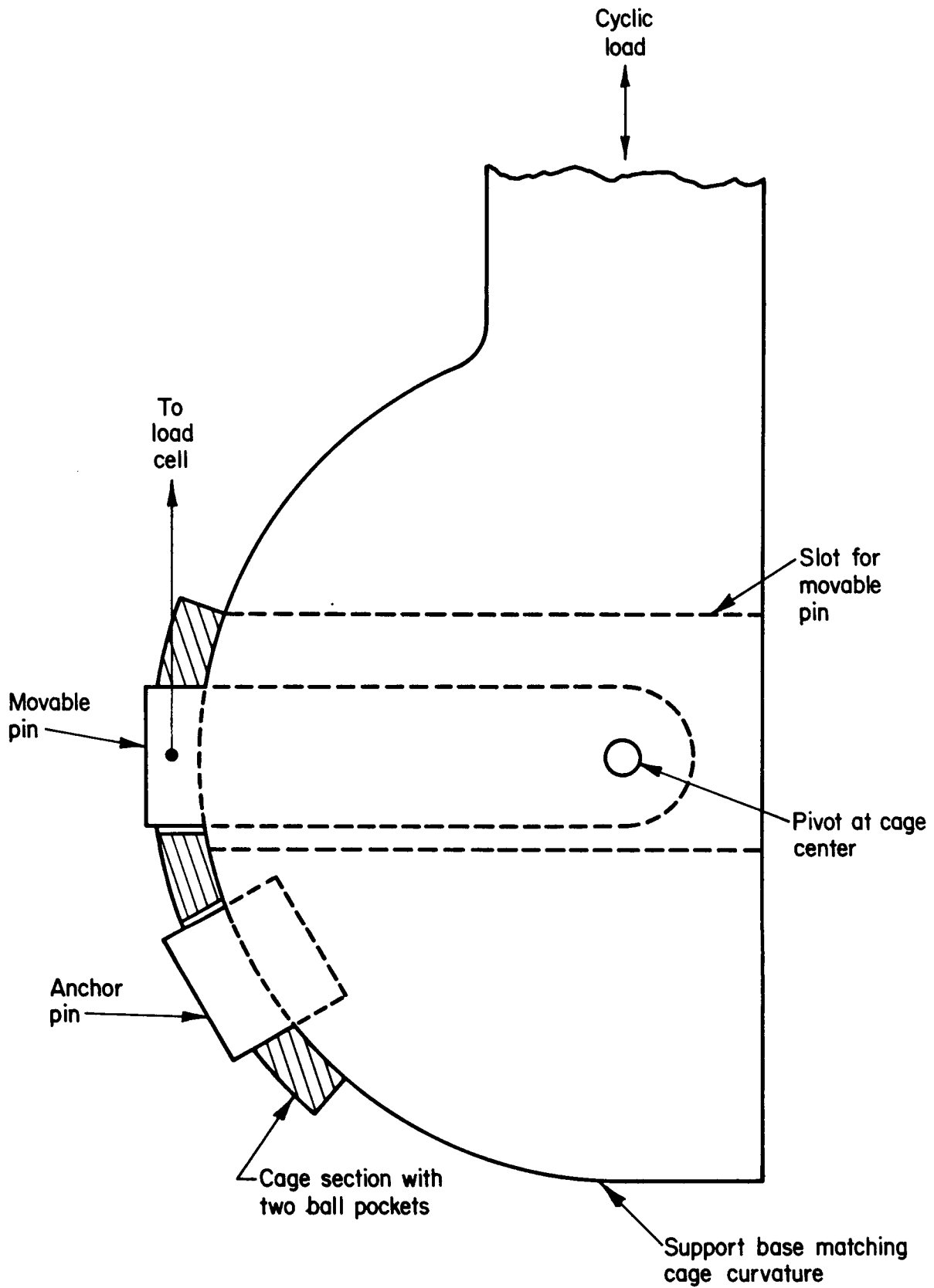Support base matching
cage curvature

FIGURE 14. EXPERIMENTAL ARRANGEMENT FOR EVALUATING THE EFFECT OF
CYCLIC LOADING ON SECTIONS OF CAGE FROM THE SSME HPOTP
BEARINGS

The fatigue machine was programmed to run in load control, which sinusoidally varies the preselected loads from the minimum to maximum levels at whatever deflection is required. The tests were restricted to tensile loads with the minimum set at 133 N (30 lbs) to avoid motion caused by the lash in the system. A frequency of 6 to 7 Hz was found to be the maximum attainable without inducing undesirable secondary vibrations.

Results of Cyclic Loading Tests

The results of the cyclic loading tests are presented in Table 8. The average ultimate tensile strength measured on three baseline (no cyclic loading) specimens was 4760 N (1070 lbs). An attempt to test a cyclically loaded specimen at approximately 47 percent of this average strength, 2220 N (500 lbs), resulted in a failure at 11,390 cycles. The remaining tests were run with cyclic-load maximums of 1330 N (300 lbs) and 1780 N (400 lbs). These levels correspond to 28 percent and 37 percent of the average ultimate tensile strength, respectively. Three of the four specimens tested with a cyclic-load maximum of 1330 N (300 lbs) for 125,000 cycles showed an increase in subsequent ultimate tensile strength. Specimens tested with a cyclic-load maximum of 1780 N (400 lbs) for 125,000 cycles showed a decreased in subsequent ultimate tensile strength. These changes represent an increase of 11 percent and a decrease in 8 percent of the baseline strength, respectively.

The glass fibers of the Armalon provide the primary tensile strength of the composite. Unlike a homogeneous material in which the load is distributed evenly across the stressed section, the load in a composite is applied to the individual fibers. Depending upon their orientation, straightness, and bonding to the matrix, the resulting stress will vary widely from fiber to fiber. Therefore, failure

TABLE 8. RESULTS OF CYCLIC TENSILE LOAD TESTS
ON CAGE SPECIMENS AT -196 C (-320 F)

Specimen Number	Cyclic Load Maximum for 125,000 Cycles, N(lbs)	Ultimate Tensile Strength, N(lbs)	Change from Baseline, N(lbs)	Change from Baseline, Percent
2-3	--	4840 (1088)	--	--
4-3	--	4170 (938)	--	--
5-1	--	5280 (1187)	--	--
		Avg 4760 (1070)		
2-4	1330 (300)	5400 (1213)	620 (140)	+13
4-4	1330 (300)	4170 (938)	-590 (-132)	-12
5-2	1330 (300)	5890 (1325)	1130 (255)	+24
5-3	1330 (300)	5630 (1265)	870 (195)	+18
		Avg 5270 (1190)	510 (120)	+11
3-5	1780 (400)	4060 (913)	-700 (-157)	-15
4-5	1780 (400)	4340 (975)	-420 (-95)	-9
5-4	1780 (400)	4730 (1063)	-30 (-7)	-0.7
		Avg 4370 (980)	-384 (-86)	-8
2-5	2220 (500)*	--	--	--

*Specimen failed at 11,390 cycles

during an ultimate strength tensile test is progressive as the highly
stressed fibers fracture and the load is shifted to the fibers pre-
viously having lower stress levels. Apparently the cyclic loading
at 1330 N (300 lbs) permitted movement within the matrix to improve
the load sharing among the fibers so that the subsequent tensile test
resulted in a higher ultimate strength. In contrast, the tests at
loads of 1780 N (400 lbs) and 2220 N (500 lbs) resulted in decreases
in the ultimate tensile strength or early fracture. Apparently loads
at these levels cause fracture of some of the principal load-carrying
fibers during the cycling. On this basis, the safe long-term working
tensile loads for the cage are on the order of no more than 1330 N
(300 lbs).

MEASUREMENT OF POISSON'S RATIO

Poisson's ratio measurements were performed using a rectangular bar (25.4mm (1 in.) long by 635 mm (0.25 in.) square) cut from an Armalon cylinder, with the long dimension of the bar aligned parallel to the cylinder axis. All surfaces across the plies were ground flat and parallel. Two pairs of electric-resistance strain gages were affixed to the bar, one pair on the outer surface, parallel to the plies, and the other on a through-wall surface, across the plies. Each pair consisted of one gage oriented in the axial direction of the bar and one oriented normal to the axis. The bar was loaded axially in compression with the output of each gage pair recorded on a separate x-y recorder. Poisson's ratio data were obtained at room temperature for both surfaces. The across-ply gages failed at liquid nitrogen temperature, but the parallel-to-ply gages survived.

The results were as follows:

Temperature, deg C (F)	Poisson's Ratio	
	With-Ply	Across-Ply
20 (68)	0.15	0.68
-196 (-321)	0.20	----

The across-ply value is quite high, presumably due to relatively weak bonding which allows the plies to spread apart easily in compression. This effect may not be nearly as pronounced at low temperatures, where the bonding may be stronger.

MEASURING UNITS

All of the calculations and measurements were performed using the English system of units. The SI units appearing in the report were converted from the English units.

REFERENCES

(1) Jones, A. B., "A General Theory for Elastically Constrained Ball
     and Radial Roller Bearings Under Arbitrary Load and Speed Condi-
     tions", Journal of Basic Engineering, pp 309-320, June, 1960.

(2) "High Pressure Oxygen Turbopump Bearing Cage Stability Analyses",
     Battelle Final Report to NASA for Task No. 113 on Contract NAS8-
     34908, March 8, 1984.

(3) Personal Communication with Fred Dolan, GMSFC, Sept., 1985.

(4) "Bearing Materials Studies for Space Shuttle Main Engine (SSME)
     Cryogenic Turbopump Application", Battelle Final Report to NASA
     for Task No. 115 on Contract No. NAS8-36192, May 15, 1985.

(5) "Measurements of Elastohydrodynamic Film Thicknesses, Wear, and
     Tempering Behavior of High Pressure Oxygen Turbopump Bearings",
     Battelle Final Report to NASA for Task No. 112 on Contract No.
     NAS-34908, April 2, 1984.

(6) Kannel, J. W., and Bupara, S. S., "A Simplified Model of Cage
     Motion in Angular Contact Bearings Operating in the EHD Region",
     J. Lub. Tech., Trans. ASME, Vol. 100, No. 3, July, 1978, pp 395-
     403.

(7) Kannel, J. W., and Snediker, D. K., "The Hidden Cause of Bearing
     Failure", Machine Design, April 7, 1977, pp 78-83.

(8) Kingsbury, E. P., "Torque Variations in Instrument Ball Bearings",
     ASLE Transactions, 1965, pp 435-441.

(9) Palmgren, A., Ball and Roller Bearing Engineering, 3rd Edition,
     S. H. Burbank & Co., Inc., Philadelphia, 1959, pp 21.

APPENDIX A

ANALYSIS OF TRACTION FORCES IN
A PRECISION TRACTION DRIVE

85-Trib-45

Analysis of Traction Forces in a Precision Traction Drive

J. W. Kannel

Battelle Columbus Laboratory,
Columbus, Ohio 43201

T. A. Dow

Precision Engineering Laboratory,
North Carolina State University,
Raleigh, N.C. 27695-7910

*A theory for the shear stress between a rough elastic cylinder and a cylinder with a
soft layer has been developed. The theory is based on a Fourier transform approach
for the elasticity equations coupled with surface deflection equations for transient
contacts. For thick layers (h > .001 in.) the shear stress on the surface approaches
the shear of the layer alone. The elastic shear deflection (~ 100 μin.) as a result of
the tangential load is significant and increases if a surface layer such as a thin
coating is added to one or both cylinders. The predicted interfacial shear stresses are
considerably altered by surface roughness on uncoated surfaces and these effects
are ameliorated by the addition of a thin soft surface coating.*

Introduction

Two critical aspects of a precision machine are linear
location of one part relative to another and smooth motion
between limits. One method of achieving this result [1, 2] is to
use a traction drive on the slideway as illustrated in Fig. 1.
Positioning accuracy below the microinch level is typically
required. When accuracies of this level are involved, virtually
all factors which affect motion must be considered in order to
minimize errors in the system. One such factor is the shear
deformation of the drive system, especially the elasticity of
the traction interface. The elasticity is affected by many
factors, including the Young's modulus of the traction
components, surface layers on the rollers (such as solid film
layers) and the roughness of the rollers and slideway.

The most extensive work reported on the analysis of the
traction interface is by Kalker [3, 4]. Kalker traces the traction
interface between two extremes: the Cattaneo [5] problem and
the Carter [6] problem. The Cattaneo problem occurs when a
cylinder is rotated slightly, while in contact with a stationary
surface. The Carter problem occurs when both the cylinder
and the mating surface are moving but at slightly different
speeds. Kalker's study traces the traction forces through the
transients between the two extremes.

Bentall and Johnson [7] analyzed the slip between two
dissimilar cylinders in rolling contact. This research allowed
for tangential deflections due to microslip. Barber [8] con-
ducted research similar to Kalker's, only he analyzed three-
dimensional contacts of rollers under misalignment. Poritsky
[9] derived basic equations for cylinders in contact and
discussed the problem of rough surfaces. Krause and Senuma
[10] did experimental studies with rollers which developed
surface corrugations. The surface corrugations notably af-
fected the traction behavior of the cylinders.

The work presented here is an extension of the Kalker and
Poritsky work with allowances for surface layers. The surface
layer algorithm is developed from the work of Sneddon [11],
and Gupta and Walowit [12].
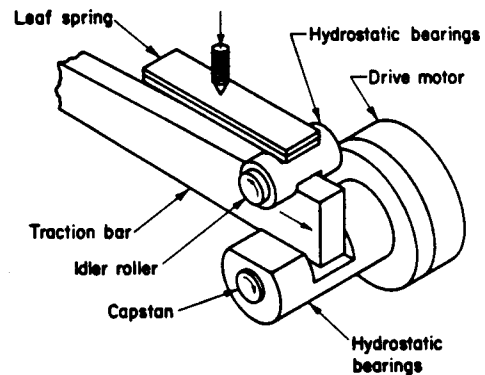
"The resolution of the slide drive will be
0.2 μin. (0.005 μm). This is the equivalent to
0.05 arc."

Fig. 1 Illustration of traction control system for precision engineering

Approach

The same general approach used for the normal stress
analysis [13] can be used for the shear stress computations. As
will be shown subsequently, the matrix equation is almost
identical to that developed by Gupta-Walowit for the normal
stress computations. That is the deformation equations can be
put in the matrix form:

$$C\bar{F} = \bar{\epsilon} \qquad (1)$$

where C is the matrix equation with elements c_{ij} that relate the
tangential deflection, $\bar{\epsilon}$, to the tangential forces. As with the
normal stress equations, a relationship between point-loads
and point stresses can be developed.

Matrix Coefficients

For a solid body, Poritsky derived a similar relationship for
load-deflection coefficients as for normal stress coefficients,
that is

$$c_{ij} = -\frac{4(1 - \nu^2)\ln}{\pi E} |r| \qquad (2)$$

Discussion on this paper will be accepted at ASME Headquarters until December 9, 1985

$$\begin{bmatrix}
1 & 0 & 1 & 0 & 0 & 0 \\
-s^2 & s & s^2 & s & 0 & 0 \\
1 & 1 & \bar{i}^2 & \bar{i}^2 & -\bar{i} & 0 \\
-z & 1-z & z\bar{i}^2 & (1+z)\bar{i}^2 & z\bar{i} & 0 \\
z(\nu_1'-1) & 3-z-\nu_1'(1-z) & (1-\nu_1')z\bar{i}^2 & [2+(1+z)(1-\nu_1')]\bar{i}^2 & (1-\nu_2')z\bar{i} & (\nu_2'-3)\gamma\bar{i} \\
(1+\nu_1'') & (1+\nu_1'')-2z/s^2 & (1+\nu_1'')\bar{i}^2 & [(1+\nu_1'')+2z/s^2]\bar{i}^2 & -(1-\nu_2'')\gamma\bar{i} & 2z\gamma\bar{i}/s^2
\end{bmatrix}$$

$$\begin{Bmatrix} A_1 \\ B_1 \\ C_1 \\ D_1 \\ A_2 \\ B_2 \end{Bmatrix} = \begin{Bmatrix} 0 \\ 1 \\ 0 \\ 0 \\ 0 \\ 0 \end{Bmatrix}$$

where
$z = |s|$ $\nu' = (2-\nu)/(1-\nu)$ $\beta = (1-\nu_3^2)E_1/(1-\nu_1^2)E_3$
$\bar{i} = \exp(z)$ $\nu'' = \nu/(1-\nu)$ $\gamma = (1-\nu_2^2)E_1/(1-\nu_1^2)E_2$

where r is the distance between a point tangential load and the corresponding tangential deflections. As with the normal stress equations, a relationship between point loads and stresses over a small region is:

$$F_i = \tau dx \tag{3}$$

where τ is the surface shear stress acting over a distance dx (or Δx in finite terminology). Then

$$c_{ij} = \frac{-4(1-\nu^2)}{\pi E} \int_{x_j-\Delta x/2}^{x_j+\Delta x/2} \ln|x_i - x| dx \tag{4}$$

which allows a solution to be found when $x_j = x_i$.

An expression has been develoepd for the influence-coefficient matrix for shear stresses in a layered solid (see Appendix A). The solution (assuming no normal pressure on the surface) can be written as:

$$c_{ij} = \frac{(1-\nu_1^2)}{\pi E} \left[\int_0^{s_0} 2(B_1-D_1)(\cos s\,\zeta - \cos s)\,ds \right. \tag{5}$$

$$\left. + 2\int_{s_0}^{\infty} \frac{\cos s\,\zeta - \cos s}{s}\,ds - 2\beta\ln\zeta \right]$$
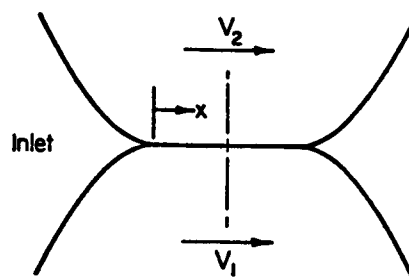
where $\zeta = |r|/h$

Fig. 2 Slippage in the contact zone

and the coefficients B_1 and D_1 are computed using the matrix of Table A1. This equation is identical to Poritsky's formulation for $s_0 = 0$.

Tangential Deflection Equations

Kalker has developed the following expression for the surface deflections:

$$V(x,t) = C_R(t) + \frac{1}{V}\frac{\partial\epsilon}{\partial t} + \frac{\partial\epsilon}{\partial x} \tag{6}$$

Nomenclature

A_1 = constant Table A1
b = half width of contact
B_1 = constant for Table A1
C_1 = constant for Table A1
D_1 = constant for Table A1
E = Young's modulus
f = coefficient of friction under slip conditions ($f = 0.3$)
$\bar{F}$ = point tangential force
F_t = tractive force
G_m = shear modulus $G_m = E/2(1+\nu)$
h = thickness of layer
p = pressure
p_h = maximum Hertz pressure
p_{max} = maximum contact pressure
r = distance from point of load application to deflection $|x_i - x_j|$

R_1, R_2 = cylinder radii
$\dfrac{1}{R} = \dfrac{1}{R_1} + \dfrac{1}{R_2}$
s = variable derived from Fourier transform
s_0 = equation (5)
$\bar{i}$ = exp(z)
t = time
u = deformation in x direction
v = deformation in y direction
V = velocity of a contact point
ΔV = slip velocity
x = coordinate direction tangential to surface
y = coordinate direction normal to surface

γ = ratio of E(layer)/E(substrate)
β = ratio of E(layer)/E(indentor)
δ_{ij} = Kronecker delta
ϵ = tangential deflection relative to a fixed point
ζ = r/h
η = y/h
ν = Poisson's ratio
ν' = $(2-\nu)/(1-\nu)$
ν'' = $\nu/(1-\nu)$
x = normal stress in tangential direction
y = normal stress in radial direction
τ = shear stress
Ψ = Airy's stress function

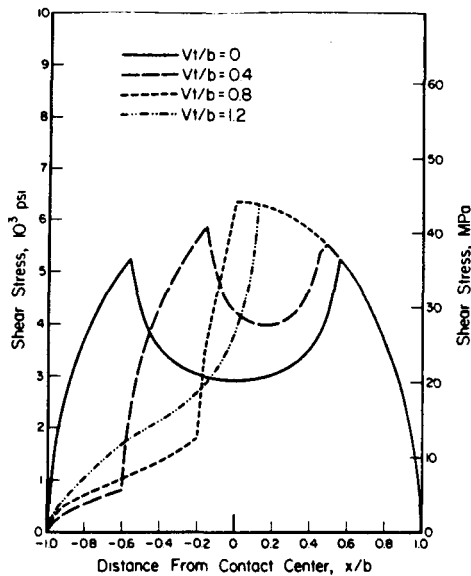**Fig. 3 Contact zone shear stress distribution (no layer)**
b = 0.25 mm (0.01 in.) $F_t/fw' \approx 0.7$
R = 9.4 mm (0.37 in.)

where

ϵ = tangential elastic deflection (of both surfaces) for a
point on the surface
V = velocity of points on the surfaces
C_R = creepage
$x = x$ position
t = time

Kalker's expression was designed for use in analytical expressions. For numerical computations, it is desirable to develop a somewhat different expression.

Assume that the lower surface in Fig. 2 is moving slower (velocity = V_1) than the upper surface (velocity = V_2); and, for the first step in the iteration, that no slip occurs in the interface. Based on these assumptions the deflection of a point in the interface at a new time ($t + \Delta t$) can be written

$$\epsilon(x + V\Delta t, t + \Delta t) = \epsilon(x,t) + \Delta V \Delta t \qquad (7)$$

Note the point itself has advanced $V \Delta t$ and the deflection has increased by an amount $\Delta V \Delta t$. If the left side of this expression is expanded in a Taylor series we have

$$\epsilon(x,t) + \frac{\partial \epsilon}{\partial x} V\Delta t + \frac{\partial \epsilon}{\partial t} \Delta t = \epsilon(x,t) + \Delta V \Delta t \qquad (8)$$

or

$$\frac{\partial \epsilon}{\partial x} + \frac{1}{V} \frac{\partial \epsilon}{\partial t} = \frac{\Delta V}{V} \qquad (9)$$

where

$\Delta V = V_2 - V_1$

$V = V_1$

This expression is consistent with Kalker's equation. For the steady state situation, equation (9) becomes

$$\epsilon = \frac{\Delta V}{V} x + C_{R1} \qquad (10)$$

If $V_1 = 0$ in equation (9), the horizontal deformation becomes:

$$\epsilon = V_{2t} + CR2 \qquad (11)$$

To compute the elastic deflections at any time the deflection at a previous time must be known. Many of the calculations were performed using equation (11) for the tangential deflection at $t = 0$. The time transient problem when both cylinders move was analyzed using equation (7).

Solution Technique

The method of solution involves solving equation (1) with equation (5) in the form (see Appendix)

$$\sum_{j=1}^{n} (c_{ij} - c_{0j}) \tau_j \Delta x = \epsilon_i(t) \qquad (12)$$

where $\epsilon_i(0)$ is the assumed initial deflection relative to a fixed point ($x_0 = -10b$). For subsequent times equation (7) is used with $\Delta V \Delta t$ being a constant that is added to each time step to produce a given traction.

In the computations the coefficients c_{ij} were set and the shear stress computed by a matrix solution of equation (12). At some points

$$\tau_j > f \cdot p_j$$

where f is a coefficient of friction and p_j is the local pressure computed using the technique given in reference [12 and 13]. For these points the matrix was adjusted as follows:

$$\sum_{j=1}^{n} (1 - \delta_{jjf}) (c_{ij} - c_{0j}) \tau_j \Delta x = \epsilon_i$$

$$- \sum_{j=1}^{n} \delta_{jjf} fp_j (c_{ij} - c_{0j}) \tau_{jf} = fp_{jf} \qquad (13)$$

where

$$\delta_{jjf} = \begin{cases} 0 j \neq j_f \\ 1 j = j_f \end{cases}$$

j_f are the points where $\tau_j > fp_j$. The essential size of the matrix will be reduced by one row for each value of j_f. The computations involved a simple iteration starting with a full matrix and subsequently reducing the matirx for each value of $\tau_j > fp_j$ until further iterations produced no changes.

Discussion

Figure 3 illustrates the shear stress at the interface for the case of a stationary lower cylinder ($Vt/b = 0$) and for a series of relative slip values ($Vt/b > 0$). The slip values are expressed in terms of the half width, b. If $Vt/b = 0.8$, a point on the upper cylinder has moved a distance equivalent to 80 percent of the half-width of contact between the cylinders.

For the case of a stationary lower disk (analogous to the Cattaneo problem), the shear stresses are the lowest in the center of contact and rise toward the edges. This rise is due to the contribution of each element to support the shear deformation outside the contact region. The rise in shear stress is limited at $x/b \cong \pm 0.7$ by slip between the cylinder surfaces; that is, the shear stress becomes equal to the friction coefficient times the normal stress. Thus, the shear stress curve has the same shape as the normal stress distribution where slip is present. For this example the horizontal load was 105 N/mm (600 lb/in.), and to produce this force, the upper cylinder was rotated 2×10^{-4} rad (the upper surface moved 2 μm).

Continued rotation of the upper cylinder would produce rotation of the lower disk because the loading was assumed to remain constant (analogous to Carter problem). Different values of the upper cylinder motion are also illustrated in Fig. 3. For the largest rotation of the upper cylinder shown in Fig. 3 ($Vt/b = 1.2$, corresponding to 3.2×10^{-2} rad (about 2 deg) of rotation), a point on the upper cylinder has moved a total of 2.5 μm from a point on the lower cylinder which was adjacent at no load. This means that the driving cylinder will rotate 2.7×10^{-4} rad more than the driven cylinder for an average rotation of 3.2×10^{-2} rad against a load of 600 lb.
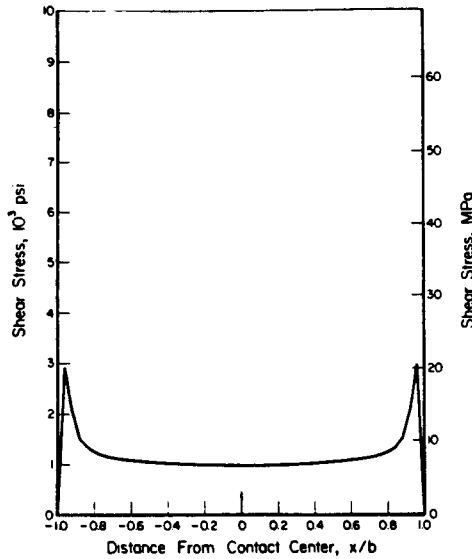
One purpose of the analytical traction model was to

Fig. 4 Contact zone shear stress distribution (0.01 in. layer)
$b = .89$ mm (.035 in.)   Load = 543 N/mm (3099 lb/in.)
$F_t = 14.5$ N/mm (83 lb/in.) $R = 9.44$ mm (.37 in.)
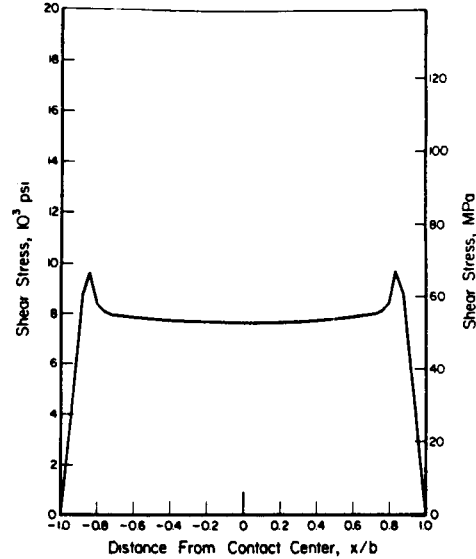$E_1 = 2$ GPa (290 ksi) $p_h = .44$ GPa (64 ksi)
$\epsilon = 2.5$ μm (100 μin.)

Fig. 5 Contact zone shear stress distribution (1000 in. layer)
$b = .44$ mm (.0173 in.)   Load = 490 N/mm (2800 lb/in.)
$F_t = 45$ N/mm (258 lb/in.) $R = 9.4$ (.37 in.)
$E = 2$ GPa (290 ksi) $p_h = .8$ GPa (117 ksi)
$\epsilon = 2.5$ μm (100 × 10^6 μin.)

evalaute the role of surface layers on traction drive performance. Figures 4 to 6 show the shear stress distribution for the condition of a uniform tangential displacement of 2.5 μm but with a soft surface layer (E = 2 GPa) on one of the cylinders. Surface layer thicknesses of 250 μm, 25 μm and 2.5 μm are illustrated.

All curves show peak shear stresses at the edges of contact and reasonably uniform shear stress in the center. For the thicker layers this center shear stress should approach the shearing of a soft layer of known thickness a known amount. That is:

$$\tau = G_m \bar{\gamma} = G_m \epsilon / h \qquad (14)$$

where

$\bar{\gamma}$ is the shear strain
G_m is the shear modulus of the layer ($G_m = E/2(1 + \nu) = 780$ MPa)

For the 250 μm layer shown in Fig. 4, the predicted shear stress using equation 14 is 7.8 MPa (1.125 ksi). This predicted stress is consistent with the stress near the center of contact of Fig. 4. At the edges of the contact ($x = b$) the stress rises considerably above this level to compensate for the forces required to tangentially deflect the layer outside of the contact region. Very near the edges, the shear stress is limited by the coefficient of friction times the normal pressure.

In Fig. 5 the predicted shear stress using equation (14) would be 78 MPa (11.25 ksi). This stress is higher than the stress at the center of contact given in Fig. 5. That is, for thin films, the shear stresses tend to be high enough to deflect the substrate as well as the surface. When the substrate is deflected this deflection must be subtracted from ϵ in computing the surface shear. For very thin films ($h = 2.5$ μm) as shown in Fig. 6 the center shear stress is considerably lower than predicted by shearing of the layer alone. For this case the equation (14) shear stress would be 780 MPa (112.5 ksi) or about four times that given in Fig. 6. Clearly then the evaluation of this surface films requires the use of comprehensive theories and cannot be achieved by simple analyses.

Figures 7 and 8 illustrate the comparison between a layered and a nonlayered body. For the conditions given here a surface "wind-up" of 2.5 μm produces a tangential load of 105 N/mm when the soft layer (E = 2 GPa) is in place. If there were no layer, 105 N/mm could be obtained with a
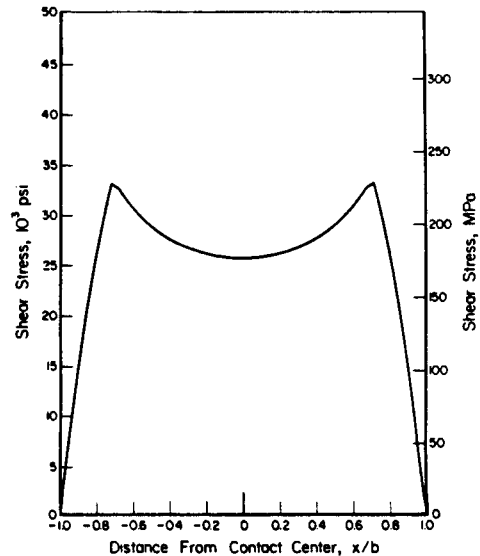

Fig. 6 Contact zone shear stress distribution (100 μ in. layer)
$b = .29$ mm (.0115 in.)   Load = 544 N/mm (3110 lb/in.)
$F_t = 103$ N/mm (591 lb/in.) $R = 9.4$ mm (.37 in.)
$E = 2$ GPa (290 ksi) $p_h = 1.28$ GPa (187 ksi)
$\epsilon = 2.5$ μm (100 μin.)

"wind-up" of 2 μm, as indicated in Fig. 8. The presence of the soft layer also increases the amount of "wind-up" required to move the driven cylinder against the load. For example, for the bare cylinder (Fig. 8) a "wind-up" of 2.5 μm occurs in traversing through 1.2 half widths 0.3 mm). For the layered cylinder (Fig. 3) a "wind-up" of 3.5 μm occurs in traversing the same distance.

For the above examples the surface of the drive cylinder would move 2.5 μm farther than the driven cylinder over 0.3 mm traverse. If one of the cylinders contained a soft layer the differential traverse would be increased by about 1 μm. In a precision control system, all errors must be minimized to reduce the level of error compensation required of the control system. Based on error minimization alone then, it would seem that bare cylinders would be superior to coated cylinders. However, when surface roughness factors are included
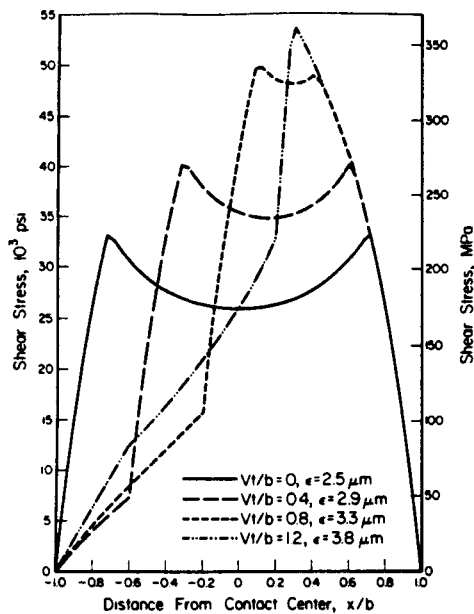
Fig. 7 Contact zone shear stress distribution (100 μ in. layer)
$b = .29$ mm (.0115 in.)   Load = 544 N/mm (3110 lb/in.)
$F_t = 105$ N/mm (600 lb/in.) $R = 9.4$ mm (.37 in.)
$D = 2$ GPa (290 ksi) $p_h = 1.28$ GPa (187 ksi)

Fig. 9 Shear stress distribution with 1 μ in. CLA surface roughness (no layer)
$b = .25$ mm (.01 in.)   Load = 639 N/mm (3649 lb/in.)
$F_t = 105$ N/mm (600 lb/in.) $R = 9.4$ mm (.37 in.)
$E = 200$ GPa (29M psi) $p_{max} = 2$ GPa (295 ksi)
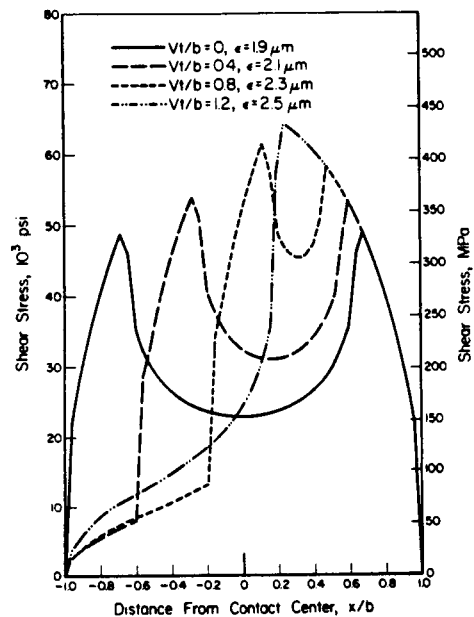$\epsilon = 1.9$ μm (75 μin.)

Fig. 8 Contact zone shear stress distribution (no layer)
$b = .25$ mm (.01 in.)   Load = 607 N/mm (3470 lb/in.)
$F_t = 105$ N/mm (600 lb/in.) $R = 9.4$ mm (.37 in.)
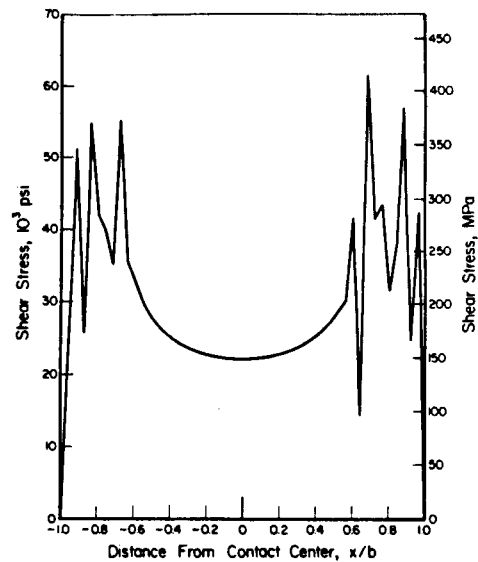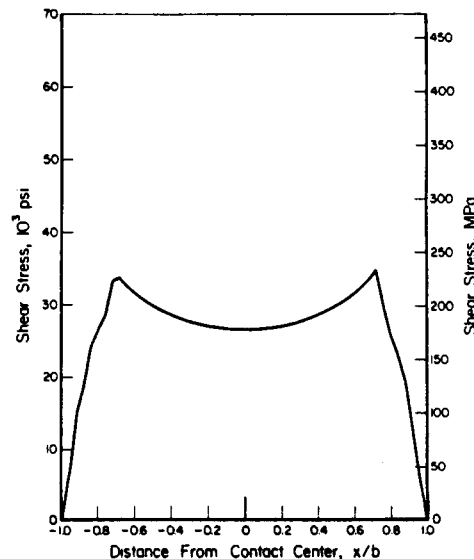$E = 200$ GPa (29M psi) $p_h = 1.5$ GPa (219 ksi)

Fig. 10 Shear stress distribution with 1 μ in. CLA surface roughness (100 μ in. layer)
$b = .29$ mm (.0115 in.)   Load = 545 N/mm (3114 lb/in.)
$F_t = 100$ N/mm (601 lb/in.) $R = 9.4$ mm (.37 in.)
$E = 2$ GPa (29 ksi) $p_{max} = 1.33$ GPa (195 ksi)
$\epsilon = 2.5$ μm (100 μm)

in the shear stress examinations the value of a surface layer becomes clear. Figure 9 indicates the shape of the shear stress distribution for a stationary lower cylinder without a layer but with a 0.025 μm center line average (cla) surface roughness. The increased deformations due to the surface roughness produces peaks in the shear stress distribution in the slip regions ($x/b > \pm 0.7$). The addition of a soft, thin layer (2.5 μm) cushions the surface asperities and produces a smoother shear stress curve as indicated in Fig. 10. Based on the results of Figs. 9 and 10, it would be difficult to compensate for the erratic stresses for a nonlayered cylinder. However, it is quite reasonable to attempt to predict the stresses where a layer is present.

Conclusions

Traction drive systems represent reasonable devices for traversing slideways in precision machining. However, one inherent problem with traction is that the traction interface must incur sizable elastic "wind-up" before the driven cylinder will move against a given load. For one specific case analyzed the "wind-up" was on the order of 2 μm for a 105 N/mm traction load. The amount of "wind-up" increased as the driven cylinder moved.

In order to achieve precision control in a traction drive, some type of compensation algorithm must be employed to eliminate "wind-up" errors. It would be expected that a compensation algorithm of the type presented herein could be employed provided good reproducibility of the traction in-

terface could be achieved. One problem in reproducibility is surface roughness. Even small levels of roughness (0.025 μm cla) can cause wild variations in interfacial shear stresses. A thin coating such as a 2.5 μm molybdenum disulfide coating can absorb the roughness and create a much smoother (and hence more reproducible) shear stress distribution. The presence of the soft layer would cause a slight (~0.6 μm) increase in "wind-up" but presumably the "wind-up" would be predictable.

References

1 Bryan, J. B., "Design and Construction of an Ultraprecision 84 Inch Diamond Turning Machine," *Precision Engineering*, Vol. 1, No. 1, 1979, pp. 13-17.

2 Barkman, W. E., "Machine and Tool Drive System," *Precision Engineering*, Vol. 2, No. 3, 1980, pp. 141-146.

3 Kalker, J. J., "Transient Rolling Contact Phenomena," *Trans. ASLE*, Vol. 14, 1971, pp. 177-184.

4 Kalker, J. J., "Rolling With Slip and Spin in the Presence of Dry Friction," *Wear*, 9, 1966, pp. 20-38.

5 Cattaneo, C., "Sul Contatto di du Corpi Elastici: Destribuzione Locale Degli Sfoizi," *Rend. Acad. Lincei*, Series 6, Vol. 27, 1938, pp. 342-348, 434-436, 474-478.

6 Carter, F. W., "On the Action of a Locomotive Driving Wheel," *Proc. Royal Soc.*, a 112, 1926, pp. 151-157.

7 Bentall, R. H., and Johnson, K. L., "Slip in the Rolling Contact of Two Dissimilar Elastic Rollers," *J. Mech. Eng. Sci.*, Vol. 9, 1967, pp. 389-404.

8 Barber, J. R., "The Rolling Contact of Misaligned Elastic Cylinders," *J. Mech. Eng. Sci.*, (I. Mech. E.), Vol. 22, No. 3, 1980, pp. 125-128.

9 Poritsky, H., "Stress and Deflections of Cylindrical Bodies in Contact With Application to Contact Gears and Locomotive Wheels," ASME *Journal of Applied Mechanics*, 1950, pp. 191-201.

10 Krause, H., and Senuma, T., "Investigation of the Influence of Dynamic Forces on the Tribological Behavior of Bodies in Rolling/Sliding Contact With Particular Regard to Surface Corrugations," ASME JOURNAL OF LUBRICATION TECHNOLOGY, Vol. 103, 1981.

11 Sneddon, I. N., *Fourier Transforms*, McGraw-Hill, 1951.

12 Gupta, P. K., and Walowit, J. A., "Contact Stresses Between a Cylinder and a Layered Elastic Solid," ASME JOURNAL OF LUBRICATION TECHNOLOGY, Apr. 1974, pp. 250-257.

13 Kannel, J. W., and Dow, T. A., "Evaluation of Contact Stresses Between a Rough Elastic and a Layered Cylinder," to be presented at the Leeds-Lyon Conference, Sept. 1985.

APPENDIX

Development of Shear-Deflection Equations

Fourier Transform Equation. The objective of this analysis is to develop a relationship between surface shear stresses and tangential deflections in absence of applied normal stresses at the boundary. The analyses are based on elasticity theory using the Fourier transform approach given by Sneddon and Gupta and Walowit. These equations are given in the following form (see Fig. A1).

$$\sigma_y = \frac{\partial^2 \Psi}{\partial x^2} = -\frac{1}{2\pi} \int_{-\infty}^{\infty} \omega^2 \bar{G} \exp(-i\omega x) d\omega$$

$$\sigma_x = \frac{\partial^2 \Psi}{\partial y^2} = \frac{1}{2\pi} \int_{-\infty}^{\infty} \frac{d^2 \bar{G}}{dy^2} \exp(-i\omega x) d\omega$$

$$\tau_{xy} = -\frac{\partial^2 \Psi}{\partial x \partial y} = \frac{1}{2\pi} \int_{-\infty}^{\infty} i\omega \frac{d\bar{G}}{dy} \exp(-i\omega x) d\omega \qquad (A1)$$

$$v = \frac{1-\nu^2}{2\pi E} \int_{-\infty}^{\infty} \left[\frac{d^3 \bar{G}}{dy^3} - \left(\frac{2-\nu}{1-\nu}\right) \omega^2 \frac{d\bar{G}}{dy} \right] \exp(-i\omega x) \frac{d\omega}{\omega^2}$$

$$u = \frac{1-\nu^2}{2\pi E} \int_{-\infty}^{\infty} \left[\frac{d^2 \bar{G}}{dy^2} + \left(\frac{\nu}{1-\nu}\right) \omega^2 \bar{G} \right] i \exp(-i\omega x) \frac{d\omega}{\omega}$$

where Ψ is the Airy stress function which satisfies the biharmonic equation and G is the Fourier transform of Ψ, that is
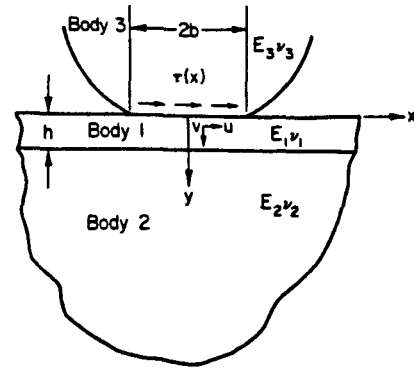
$$\nabla^4 \Psi = 0 \qquad (A2)$$

and

Fig. A1   Coordinate system for shear stress analysis

$$\bar{G} = \int_{-\infty}^{\infty} \Psi \exp(i\omega x) dx \qquad (A3)$$

Eliminating Ψ from the above two equations and solving the resulting differential equation in $\bar{G}$, we get a solution of the form

$$\bar{G} = (A + By)\exp(-|\omega|y) + (C + Dy)\exp(|\omega|y) \qquad (A4)$$

where A, B, C, and D are constants of integration to be evaluated at the boundary.

Boundary Conditions

The boundary conditions for the traction analysis are:

1) boundary stress is the applied shear stress
2) stress and deflections are continuous across the layer interface
3) stress goes to zero at $y \to \infty$;

at the surface,

$$\tau_{xy} = -\frac{\partial^2 \Psi}{\partial x \partial y} = +\frac{1}{2\pi} \int_{-\infty}^{\infty} i\omega \frac{d\bar{G}}{dy} \exp(-i\omega x) d\omega \qquad (A6)$$

If $\dfrac{d\bar{G}}{dy}$ is an odd function, Sneddon shows that:

$$\tau_{xy} = -\frac{1}{\pi} \int_0^{\infty} \omega \frac{d\bar{G}}{dy} \cos \omega x \, d\omega \qquad (A7)$$

Based on Fourier Transform theory;

$$\omega \frac{d\bar{G}}{dy} = -\int_0^{\infty} \tau xy \cos \omega x \, dx \qquad (A8)$$

at the surface $y = 0$ $\tau_{xy} = -\tau_0$. Letting τ_0 be defined over the interval Δx and letting $\tau_0 = 1/\Delta x$ then $\lim_{\Delta x \to 0}$ we have

$$\omega \frac{d\bar{G}}{dy} = 1 \qquad (A9)$$

Letting $s = h\omega$, $G = \bar{G}/h^2$, $\eta = y/h$, the first boundary condition becomes

$$s \frac{dG}{d\zeta} = 1 \quad \text{for} \quad \eta = 0 \qquad (A10)$$

Also for the case of no normal stress on the surface

$$G = 0 \qquad (A11)$$

Equations (A4), (A10), and (A11) combine to yield

$$A_1 + C_1 = 0$$

$$-A_1 s^2 + B_1 s + C_1 s^2 + D_1 s = 1 \qquad (A12)$$

where the constant in this equation are defined in body 1 of Fig. 1.

The remaining boundary conditions can be met using the same approach as used for the normal stress conditions [12]. These conditions yield the matrix given in Table A1.

Green's Function for Shear

The tangential deflection on the surface from equation (A1) can be expressed as:

$$u = -\frac{(1-\nu^2)}{\pi E} \int_0^\infty \frac{d^2 G}{d\eta^2} \frac{\cos s\zeta}{s} ds \qquad (A13)$$

where

$$\frac{d^2 G}{d\eta^2} = -2(B_1 - D_1)s \qquad (A14)$$

The Green's function can be written with reference to an arbitrary displacement V_1 at $\zeta = 1$

$$u - u_1 = \frac{1-\nu^2}{\pi E} \left\{ \int_0^\infty 2(B_1 \right.$$

$$\left. - D_1)s \frac{\cos s\zeta - \cos s}{s} ds - 2\beta \ln \zeta \right\} \qquad (A15)$$

It can be shown, using the matrix in Table A1 that for larger values of s, $(B_1 - D_1) \to 1/s$. Equation (A15) can be expressed as two integrals $(0 < s < s_0)$ and $(s_0 < s)$, as given in the text.

If we let

$$c_{ij} = u - u_1$$

then this equation corresponds to equation (5) in the text.

Because the shear deformation is calculated as a relative displacement, a reference point must be selected. The displacements calculated from equation (A15) becomes small for large ζ; therefore a reasonable assumption for the reference point is 5 contact widths ($x = -10b$). Then the relative tangential deflection (ϵ_i) is:

$$\epsilon_i = \sum_{j=1}^n (c_{ij} - c_{0j}) \tau_j \Delta x \qquad (A16)$$

assuming $i = 0$ is the reference point.

REPORT DISTRIBUTION

Installation/Code	Code

National Aeronautics and Space Administration
George C. Marshall Space Flight Center
Marshall Space Flight Center, Alabama 35812

AP29-F	1*
AS24D	3
AT01	1
CC01	1
EM13B-18	1
EH12/Mr. Dolan	6 + repro
EH01/Mr. Schwinghamer	1
SA51/Dr. Lovingood	1
SA51/Mr. G. Smith	1
SA53/Mr. Lombardo	1
EE51/Mr. Goetz	1
EP21/Mr. McCarty	1
EP23/Mr. Riggs	1

Mr. Jesse L. Richey	1*

DCASMA
Attn: DCASR CLE-GDAA-J3
Defense Electronics Supply Center
Dayton, Ohio 45444

NASA Lewis Research Center
21000 Brookpark Road
Cleveland, Ohio 45135

Mr. Herbert W. Scibbe Mail Stop 23-2	1
Mr. R. W. Parker Mail Stop 23-2	1
Mr. Ned Hannum Mail Stop 501-6	1

National Aeronautics and Space Administration
NASA Headquarters
Washington, DC 20546

Mr. F. W. Stephenson Code RST-5/E	1
Dr. M. Greenfield Code RTM-6	1

NASA Scientific & Technical Information Facility	1

Attn: Accessioning Department
P.O. Box 8757
Baltimore/Washington International Airport
Maryland 21240

*Copy of letter of transmittal only.